Scientific Research Publishing

Journal of Electromagnetic Analysis and Applications, 2025, 17(2), 15-45
https://www.scirp.org/journal/jemaa
ISSN Online: 1942-0749
ISSN Print: 1942-0730

Comparative Analysis of Single-Layer and Double-Layer Windings in Three-Phase Squirrel-Cage Induction Machines Using FEA and d-q Modelling

David Yapele[1], Andre Youmssi[2], Andre Boussaibo[2], Golam Guidkaya[3], Jean Claude Kamgang[4]

[1]Department of Electrical Engineering, Energy and Automation, National School of Agro-Industrial Sciences, University of Ngaoundere, Ngaoundere, Cameroon
[2]Department of Electrical Engineering, UIT, University of Ngaoundere, Ngaoundere, Cameroon
[3]Department of Physics, Faculty of Sciences, University of Ngaoundere, Ngaoundere, Cameroon
[4]Department of Mathematics and Computer Sciences, National School of Agro-Industrial Sciences, University of Ngaoundere, Ngaoundere, Cameroon
Email: boussaibo@yahoo.fr

How to cite this paper: Yapele, D., Youmssi, A., Boussaibo, A., Guidkaya, G. and Kamgang, J.C. (2025) Comparative Analysis of Single-Layer and Double-Layer Windings in Three-Phase Squirrel-Cage Induction Machines Using FEA and d-q Modelling. *Journal of Electromagnetic Analysis and Applications*, **17**, 15-45.
https://doi.org/10.4236/jemaa.2025.172002

Received: February 5, 2025
Accepted: February 25, 2025
Published: February 28, 2025

Abstract

This paper presents a comprehensive multi-method comparative study on the influence of single-layer and double-layer winding configurations on the static performance of three-phase squirrel-cage induction machines. By integrating high-fidelity finite element analysis (FEA) with dynamic modeling in the d-q reference frame using the Park transformation, we quantify their effects on magnetic flux distribution, magnetizing and leakage inductances, and core saturation behavior. The results reveal that double-layer windings provide superior flux homogeneity and improved inductive linearity, thus simplifying vector control. Despite increased manufacturing complexity and higher end-winding losses, this configuration improves overall electromagnetic performance, justifying its suitability for industrial applications requiring high efficiency and torque stability.

Keywords

Induction Machine, Winding Configuration, Finite Element Analysis, d-q Model, Flux Distribution, Saturation

1. Introduction

In a context where three-phase induction machines play an essential role thanks to their robustness and energy efficiency in special fields where loads are variable and sometimes require very precise controls [1] [2], like the agro-industries which use special specific applications such as conveyors, grinders or pumps [3] [4], this field of three-phase induction motors requires a constant quest for improved efficiency, power density and reliability [5]-[7]. To achieve these objectives, the design of the stator windings is an essential lever [8]. Recent research explores a wide range of approaches, from modifying traditional winding topologies to introducing unconventional configurations, optimising parameters and control techniques [9] [10]. Particular attention is paid to winding topologies, with a comparison between single-layer and double-layer configurations [6]. While single-layer windings are distinguished by their simplicity of manufacture and low cost [11], double-layer windings offer improved magnetic flux distribution and reduced space harmonics [12]. The concentric configuration is gaining popularity [13]-[15] due to reduced joule losses and increased power density. However, this approach can lead to increased harmonics and torque pulsations, requiring appropriate control strategies [16]. The use of fractional windings, although complex to manufacture, enables fine optimisation of the winding factor and a reduction in harmonics [17]. Harmonic reduction is a major issue in the design of stator windings. Several studies [6] [11] [12] show that the choice of winding topology has a significant impact on the harmonic content of the magnetic field and therefore on iron losses and rotor losses. The use of sinusoidal windings [18] and harmonic compensation techniques [19] are being explored to minimise losses and improve overall motor efficiency. However, harmonic reduction can sometimes be at the expense of the fundamental winding factor, requiring a trade-off between reducing losses and maximising torque [9]. Various optimisation techniques are used to explore the solution space and identify optimal winding configurations. Some studies [20] use stochastic optimisation algorithms, such as particle swarm optimisation (PSO), to determine optimal observer and controller gains. Other approaches combine harmonic winding analysis with multi-objective genetic algorithms to find optimal configurations based on user-defined performance objectives [13]. It is important to emphasise that the complexity of the models and optimisation algorithms must be adapted to the objectives being pursued, taking into account the trade-offs between the accuracy of the results and the computation time. However, these studies have often been limited to isolated analyses (either using finite elements to capture saturation phenomena locally, or using dynamic models to assess global characteristics), without establishing an integral link between local saturation phenomena and global parameters such as inductances. This raises the question of how to optimise the configuration of the windings in order to obtain a homogeneous distribution of flux and progressively evolving inductances, while strictly complying with identical sizing conditions for the quantity of copper. The aim of this work is therefore to develop an integrated approach aimed at rigorously comparing single layer and double-layer winding configurations, bearing in mind that the double-layer solution will make it possible to attenuate the effects of saturation and to obtain a smoother variation in inductances as the supply current increases. Our approach is distinguished first and foremost by its multi-scale integration, which combines highly detailed finite element modelling (FEA) capable of capturing local effects, in particular saturation at the edges of slots, with a dynamic model in the d-q domain enabling the extraction and quantitative analysis of global parameters such as magnetisation inductances. Furthermore, by rigorously comparing single-layer and double-layer configurations under identical sizing and copper loading conditions, we isolate the intrinsic effect of winding topology on flux distribution. Furthermore, our method allows a fine analysis of the saturation phenomena by precisely extracting the differential variations of the forward inductances L_{sd} and quadrature inductances L_{sq} from the FEA results, then integrating them into the d-q model, we offer an in-depth quantification of the saturation effects, a crucial step for the optimisation of electromagnetic performance. Finally, in a departure from traditional, exclusively qualitative approaches, our approach offers quantitative recommendations for optimising winding design, illustrating in concrete terms how improved flux distribution can mitigate saturation effects and improve overall motor stability.

2. Materials and Methods

2.1. Presentation of the Three-Phase Squirrel Cage Induction Machine and Fundamental Principle of Electromagnetic Torque Generation

1) Presentation of the Three-Phase Squirrel Cage Induction Machine

Figure 1 illustrates the complete configuration of an induction machine, which essentially comprises a stationary component the stator separated from the rotating component the rotor by a narrow air gap, the space between the stator and the rotor [21] [22].

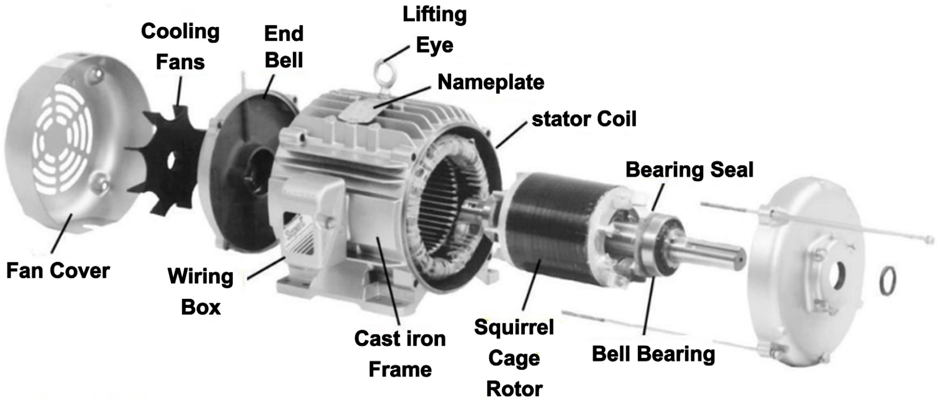

Figure 1. Parts of squirrel cage induction motor [21] [23].

2) Fundamental Principle of Electromagnetic Torque Generation

Figure 2 presents the fundamental principle of electromagnetic torque generation; the three-phase asynchronous machine is a rotating electrical machine whose static part produces a magnetic field with p pairs of poles rotating at synchronous speed when connected to the three-phase grid at frequency fs. Its moving part then rotates at a slightly different speed to that of the rotating field, hence the name asynchronous. The rotor windings are connected to themselves. The asynchronous motor therefore has neither an excitation winding nor permanent magnets [23] [24]. The rotor flux required to generate electromagnetic torque is produced from induction.

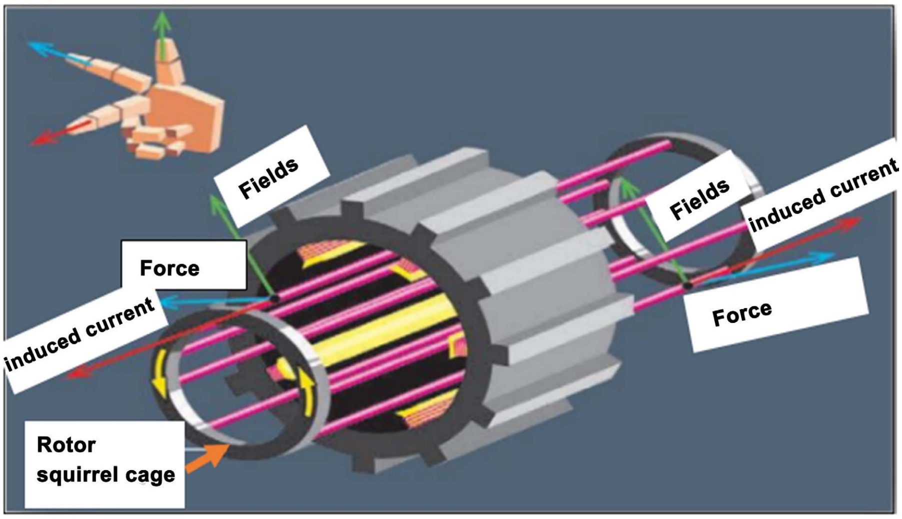

Figure 2. Principle of electromagnetic torque generation [25].

The rotor has a magnetic moment shown in black, and the stator carries three-phase windings which create a rotating field shown in green in the machine's air gap [26]. The speed of rotation depends on the frequency of the stator currents and the number of magnetic pole pairs in the machine. Design parameters such as slot opening, coil pitch and number of layers determine core losses, leakage reactance and, consequently, overall efficiency and static performance.

2.2. Modelling of the Squirrel Cage Induction Machine

Two complementary models are used to study the influence of windings on static performance: a finite element model (FEA) and a dynamic model (d-q) [27]-[29].

2.2.1. Finite Element Model of the Three-Phase Squirrel-Cage Induction Machine

The Finite Element Model discretizes the cross-section of the machine to solve Maxwell's fundamental equations in the magnetic network in the following steps [30]-[34]:

Stage 1: Writing Maxwell's fundamental equations

$$\nabla \cdot \boldsymbol{B} = 0 \tag{1}$$

(Maxwell Gauss: The divergence of the magnetic field $\boldsymbol{B}$ is zero, indicating the absence of magnetic monopoles.)

$$\nabla \times \boldsymbol{E} = -\frac{\partial \boldsymbol{B}}{\partial t} \tag{2}$$

(Maxwell Faraday "curl": the rotational electric field $\boldsymbol{E}$ is related to the time variation of $\boldsymbol{B}$.)

$$\nabla \times \boldsymbol{H} = \boldsymbol{J} \tag{3}$$

(Maxwell-Ampere (quasi-static): The magnetic field rotational $\boldsymbol{H}$ gives current density $\boldsymbol{J}$.)

$$\boldsymbol{B} = \mu \boldsymbol{H} \tag{4}$$

(Constitutive relationship for a linear medium this algebraic relationship links the fields $\boldsymbol{B}$ and $\boldsymbol{H}$ via the permeability μ without any derivation)

Stage 2: Switch to vector potential formulation

To automatically satisfy $\nabla \cdot \boldsymbol{B} = 0$, we define the vector potential $\boldsymbol{A}$ such that $\boldsymbol{B} = \nabla \times \boldsymbol{A}$ (using the rotational operator, denoted ∇). In a 2D analysis (cross-section of the machine), it is assumed that the solution depends only on the spatial variables x and y and that the field is perpendicular to the plane. We then write: $\boldsymbol{A}(x, y) = \begin{pmatrix} 0 \\ 0 \\ A_z(x, y) \end{pmatrix}$ where $A_z(x, y)$ is the only non-zero component (the magnitude $A_z(x, y)$ remains scalar, but is part of the vector potential $\boldsymbol{A}$).

Step 3: Deduce the governing equation $A_z(x, y)$

Combining Ampère's law and the constitutive relation (with $\boldsymbol{H} = \boldsymbol{B}/\mu$), and substituting $\boldsymbol{B} = \nabla \times \boldsymbol{A}$, we obtain: $\nabla \times \left(\frac{1}{\mu} (\nabla \times \boldsymbol{A}) \right) = \boldsymbol{J}$. For $\boldsymbol{A}(x, y) = (0, 0, A_z(x, y))$, the double rotational can be simplified to a scalar equation: $-\nabla \cdot \left(\frac{1}{\mu} \nabla A_z(x, y) \right) = J_z(x, y)$, using the gradient operator (∇A_z) and then the divergence operator ($\nabla \cdot$). Here, $J_z(x, y)$ denotes the z component of the current density $\boldsymbol{J}$.

Step 4: Switch to the weak formulation

Multiply the strong equation by a test function $v(x, y)$ and integrate over the domain Ω: $-\int_\Omega v(x, y) \nabla \cdot \left(\frac{1}{\mu} \nabla A_z(x, y) \right) \mathrm{d}\Omega = \int_\Omega v(x, y) J_z(x, y) \mathrm{d}\Omega$. Applying integration by parts (Green's theorem) and assuming $v(x, y) = 0$ on the edge $\partial\Omega$, we obtain: $\int_\Omega \frac{1}{\mu} \nabla A_z(x, y) \cdot \nabla v(x, y) \mathrm{d}\Omega = \int_\Omega v(x, y) J_z(x, y) \mathrm{d}\Omega$.

Step 5: Discretisation using the Galerkin method

We approximate $A_z(x, y)$ by a linear combination of functions of the form $\phi_j(x, y)$:

$A_z(x, y) \approx \sum_{j=1}^{N} \alpha_j \phi_j(x, y)$. Choosing $v(x, y) = \phi_i(x, y)$ for $i = 1, \cdots, N$, the weak formulation becomes:

$\int_{\Omega}\frac{1}{\mu}\nabla\left(\sum_{j=1}^{N}\alpha_j\phi_j\left(x,y\right)\right)\cdot\nabla\phi_i\left(x,y\right)\mathrm{d}\Omega=\int_{\Omega}\phi_i\left(x,y\right)J_z\left(x,y\right)\mathrm{d}\Omega$. Defining the stiffness matrix with $K_{ij}=\int_{\Omega}\frac{1}{\mu}\nabla\phi_j\left(x,y\right)\cdot\nabla\phi_i\left(x,y\right)\mathrm{d}\Omega$ and the source vector with $F_i=\int_{\Omega}\phi_i\left(x,y\right)J_z\left(x,y\right)\mathrm{d}\Omega$, we obtain the final linear system: $\left[K\right]\left\{\alpha\right\}=\left\{F\right\}$.

2.2.2. Dynamic Model (d-q) of the Three-Phase Induction Machine

The analytical analysis of the equations of the asynchronous machine represented in the real reference frame (a, b, c) are multivariable, non-linear and strongly coupled, making them complex to solve. We use the Park transformation to get around this problem and to obtain a system of equations with coefficients that are independent of position, thus facilitating the resolution we refer to this as the two-phase model. Figure 3 shows the Park transformation which consists of transforming the representation of the balanced three-phase motor to an equivalent two-phase representation characterised by two axes d, q [27] [35]-[42].

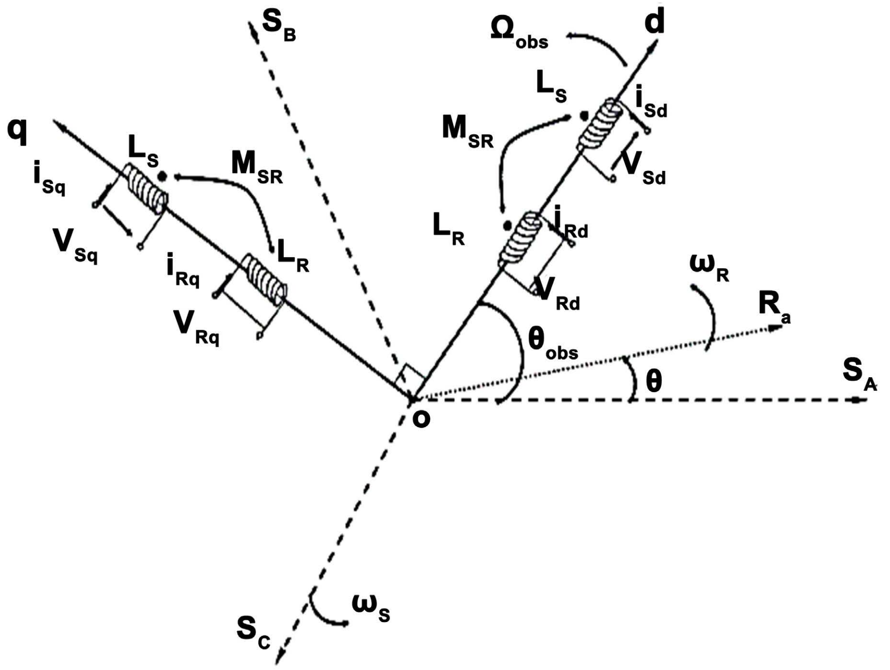

Figure 3. Angular orientation of axis systems in space [36].

The transition from a three-phase winding to a two-phase winding, taking into account the equality of the powers, is defined by the following matrix,

$$\begin{bmatrix} x_d \\ x_q \\ x_o \end{bmatrix}=\left[T_{32}\right]\begin{bmatrix} x_a \\ x_b \\ x_c \end{bmatrix} \tag{5}$$

After applying Park's transformation, the electrical and magnetic equations modelling the asynchronous motor are as follows:

$$\begin{cases} U_{sd} = r_s i_{sd} + \dfrac{\mathrm{d}\psi_{sd}}{\mathrm{d}t} - \psi_{sq}\omega_r \\ U_{sq} = r_s i_{sq} + \dfrac{\mathrm{d}\psi_{sq}}{\mathrm{d}t} + \psi_{sd}\omega_r \end{cases} \tag{6}$$

$$\begin{cases} U_{rd} = r_r i_{rd} + \dfrac{\mathrm{d}\psi_{rd}}{\mathrm{d}t} \\ U_{rq} = r_r i_{rq} + \dfrac{\mathrm{d}\psi_{rq}}{\mathrm{d}t} \end{cases} \tag{7}$$

With:

$$\begin{cases} \dot{\psi}_{sd} = L_s i_{sd} + M i_{rd} \\ \psi_{sq} = L_s i_{sq} + M i_{rq} \\ \psi_{rd} = L_r i_{rd} + M i_{sd} \\ \psi_{rq} = L_r i_{rq} + M i_{sq} \end{cases} \tag{8}$$

$$\left[V_{dq}\right] = \left[P(-\theta_e)\right] * \left[T_{32}\right]^t * \left[V_{abc}\right] \tag{9}$$

$$\left[V_{dq}\right] = [R] * \left[P(-\theta_e)\right] * \left[T_{32}\right]^t * [I] + \frac{\mathrm{d}}{\mathrm{d}t}\left(\left[P(-\theta_e)\right] * \left[T_{32}\right]^t [\varphi]\right) \tag{10}$$

$$\left[I_{dq}\right] = \left[P(-\theta_e)\right] * \left[T_{32}\right]^t * \left[i_{abc}\right] \tag{11}$$

$$\left[\varphi_{dq}\right] = \left[P(-\theta_e)\right] * \left[T_{32}\right]^t * \left[\varphi_{abc}\right] \tag{12}$$

where

$$\left[P(\theta_e)\right] = \begin{bmatrix} \cos(\theta_e) & -\sin(\theta_e) \\ \sin(\theta_e) & \cos(\theta_e) \end{bmatrix} \tag{13}$$

is the Park matrix, and

$$T_{32} = \sqrt{\frac{2}{3}} \begin{bmatrix} 1 & 0 \\ -\dfrac{1}{2} & \dfrac{\sqrt{3}}{2} \\ -\dfrac{1}{2} & \dfrac{\sqrt{3}}{2} \end{bmatrix} \tag{14}$$

In the case of a reverse passage, we have:

$$\begin{cases} \left[V_{abc}\right] = \left[P(\theta_e)\right] * T_{32} * \left[V_{dq}\right] \\ \left[I_{abc}\right] = \left[P(\theta_e)\right] * T_{32} * \left[i_{dq}\right] \\ \left[\varphi_{abc}\right] = \left[P(\theta_e)\right] * T_{32} * \left[\varphi_{dq}\right] \end{cases} \tag{15}$$

The d, q axis system is used to study transient processes in asynchronous machines with a non-symmetrical connection of the rotor circuits. For the asynchronous machine, the rotor frequency for and the angular velocity of the rotor field ω or = 2π for are zero. Consequently, the rotor voltages and currents are continuous parameters. The parameters extracted from the finite element model are fed into this dynamic model to study the influence of the windings on the magnetisation inductances and leakage reactance.

2.2.3. Coupling the Finite Element Model (FEM) and the d-q Model

Figure 4 presents the sequence we use to accurately incorporate saturation effects and magnetic heterogeneity into the dynamic simulation.

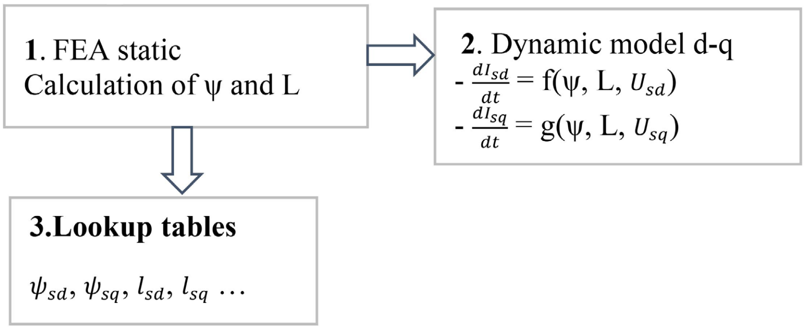

Figure 4. FEA data exchange between lookup tables and d-q model.

- Definition of a current grid (I_{sd} , I_{sq}) covering the operating envelope.
- For each point (I_{sd} , I_{sq}) 2D static finite element simulation to extract:
    - $\psi_{sd}(I_{sd}, I_{sq})$ and $\psi_{sq}(I_{sd}, I_{sq})$ (direct and quadrature flux)
    - $L_{sd}(I_{sd}, I_{sq}) = \partial\psi_{sd}/\partial I_{sd}$ and $L_{sq}(I_{sd}, I_{sq}) = \partial\psi_{sq}/\partial I_{sq}$ (differential inductances)
- Creating lookup tables
    - Organization of FEA results into 2D matrices indexed by (I_{sd} , I_{sq}).
    - Memory storage for fast bilinear interpolation.
- Online dynamic simulation
    - At each time step, the d-q model knows the instantaneous currents $I_{sd}(t)$, $I_{sq}(t)$.
    - Bilinear interpolation in tables to recover corresponding ψ_{sd}, ψ_{sq}, L_{sd}, L_{sq}.
- Solving equations of state:

$$U_{sd} = r_s i_{sd} + \frac{\mathrm{d}\psi_{sd}}{\mathrm{d}t} - \psi_{sq}\omega_r \tag{16}$$

$$U_{sq} = r_s i_{sq} + \frac{\mathrm{d}\psi_{sq}}{\mathrm{d}t} + \psi_{sd}\omega_r \tag{17}$$

With

$$\frac{\mathrm{d}\psi_{sd}}{\mathrm{d}t} = L_{sd}\frac{\mathrm{d}I_{sd}}{\mathrm{d}t} \tag{18}$$

$$\frac{\mathrm{d}\psi_{sq}}{\mathrm{d}t} = L_{sq}\frac{\mathrm{d}I_{sq}}{\mathrm{d}t} \tag{19}$$

This leads to:

$$\frac{\mathrm{d}I_{sd}}{\mathrm{d}t} = \frac{1}{L_{sd}}U_{sd} - r_s \cdot i_{sd} + \psi_{sq}\omega_r \tag{20}$$

$$\frac{\mathrm{d}I_{sq}}{\mathrm{d}t}=\frac{1}{L_{sq}}U_s-r_s\cdot i_{sq}-\psi_{sq}\omega_r \tag{21}$$

2.3. Single-Layer and Double-Layer Windings of Three-Phase Induction Machines

Establishing the windings of an asynchronous machine is based on a number of calculations and preliminary parameters that need to be known [12] [18] [43]-[45]:

2.3.1. Calculating Angles

- Mechanical angle per notch (in degrees)

$$\text{Mech Angle} = 360/\text{ns} \tag{22}$$

- Electrical angle per notch (in degrees)

$$\text{Elect Angle} = \text{mechAngle} * (\text{pôles}/2) \tag{23}$$

- Calculation of pole pitch and coil pitch
  - Number of slots per pole (for full-pitch winding)

$$\text{Pole Pitch} = \text{ns}/\text{poles} \tag{24}$$

  - No full-pitch coil

$$\text{fullCoilPitch} = \text{pôle Pitch} \tag{25}$$

  - Short-pitch coils

$$\text{Short CoilPitch} = \text{fullCoilPitch} - \text{delta} \tag{26}$$

The two most studied winding configurations are the single-layer winding and the double-layer winding, whose characteristics directly influence the static performance of the machine.

2.3.2. Single-Layer Winding

1) Single-layer winding 36 slots/2 poles

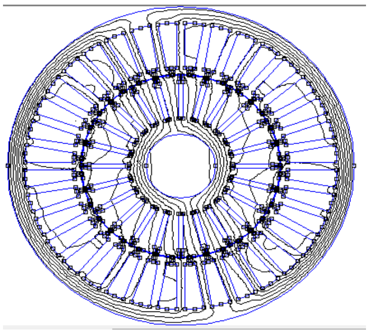

Figure 5. Magnetic field lines with 36 slots and 2 poles.

Figure 5 depicts the winding diagram for a 36-slot, 2-pole machine above consists of a symmetrical arrangement of coils, evenly distributed throughout the stator. In this system, each slot receives a portion of the windings, which ensures balanced excitation between the north and south poles and thus contributes to the creation of a stable rotating magnetic field. This configuration minimises unwanted harmonics, optimises torque development and reduces energy losses, while ensuring greater machine robustness and efficiency. The technical diagram you have provided clearly illustrates this harmonious distribution, with its concentric circles and regular angular divisions, reminding us of the precision required to build such machines.

Figure 6 presents the stator winding distribution described by a slot matrix also known as a connection matrix. This is a matrix Nph*Nd, where Nph is the number of phases and Nd is the number of slots. The elements of these vectors describe how the phases fill the stator slots, assuming a value ranging from +1 to −1.

notch 1……………………………………………………………………...notch 36

[1 1 1 1 1 1 0 0 0 0 0 0 0 0 0 0 0 0 -1 -1 -1 -1 -1 -1 0 0 0 0 0 0 0 0 0 0 0 0;

0 0 0 0 0 0 1 1 1 1 1 1 0 0 0 0 0 0 0 0 0 0 0 0 -1 -1 -1 -1 -1 -1 0 0 0 0 0 0;

0 0 0 0 0 0 0 0 0 0 0 0 1 1 1 1 1 1 0 0 0 0 0 0 0 0 0 0 0 0 -1 -1 -1 -1 -1 -1];

Figure 6. Winding connection matrix.

2) Single-layer winding 36 slots/4 poles

Figure 7 illustrates the single-layer winding produced on a stator comprising 36 slots arranged uniformly to form a 4-pole system. In this layout, each coil occupies a single slot, simplifying the manufacturing process while ensuring a balanced distribution of turns and magnetic flux. The configuration ensures that, for each pole, the slots (9 slots per pole in this case) are exploited in such a way as to optimise field density, guarantee a reduction in undesirable harmonics and promote regular and efficient torque development.

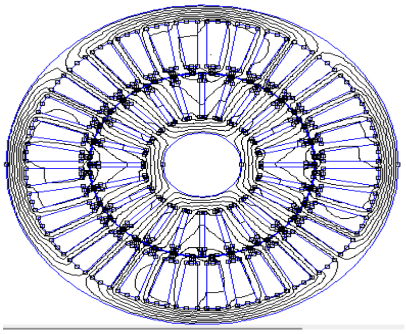

Figure 7. Single layer magnetic field lines with 36 slots and 4 poles.

Figure 8 depicts the connection matrix of a single-layer, 36-slot, four-pole stator winding. This inherently simple and geometrically symmetric topology delivers high electromagnetic performance while enabling reliable, cost-effective manufacturing. Each row of the matrix corresponds to a phase, with entries of +1 and −1 indicating coil orientation. Grouping the slots into triplets ensures precise magnetic flux balancing, thereby reducing harmonic distortion and minimizing torque ripple.

notch 1……………………………………………………………….notch 36

[1 1 1 0 0 0 0 0 0 -1 -1 -1 0 0 0 0 0 0 1 1 1 0 0 0 0 0 0 -1 -1 -1 0 0 0 0 0 0;

0 0 0 1 1 1 0 0 0 0 0 0 -1 -1 -1 0 0 0 0 0 0 1 1 1 0 0 0 0 0 0 -1 -1 -1 0 0 0;

0 0 0 0 0 0 1 1 1 0 0 0 0 0 0 -1 -1 -1 0 0 0 0 0 0 1 1 1 0 0 0 0 0 0 -1 -1 -1]

Figure 8. Winding connection matrix.

2.4. Double Layer Winding

1) Double layer winding 36 slots/2 poles

Figure 9 shows the 36-slot, two-pole double-layer winding, in which each slot contains a precisely positioned turn. Field lines, rendered as smooth curves, delineate regions of uniform, optimal magnetic flux. Geometric symmetry ensures balanced current distribution and minimizes Joule losses. This configuration promotes high starting torque and significantly reduces vibration. Graphical analysis confirms a robust structure whose meticulous design delivers superior electromagnetic performance, embodying efficiency and reliability in industrial applications.

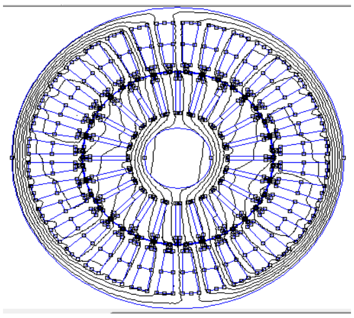

Figure 9. Double layer magnetic field lines with 36 slots and 2 poles.

Figure 10 presents the connection matrix with alternating values, where +1 denotes the incoming power supply and −1 denotes the coil current output. The top and bottom layers, corresponding to the slot subdivisions, ensure a balanced electromagnetic field distribution, thereby optimizing the winding's overall performance.

notch 1…………………………………………………………...notch 36

Lower layer = [1 1 1 1 1 1 0 0 0 0 0 0 0 0 0 0 0 0 -1 -1 -1 -1 -1 -1 0 0 0 0 0 0 0 0 0 0 0 0;

0 0 0 0 0 0 1 1 1 1 1 1 0 0 0 0 0 0 0 0 0 0 0 0 -1 -1 -1 -1 -1 -1 0 0 0 0 0 0;

0 0 0 0 0 0 0 0 0 0 0 0 1 1 1 1 1 1 0 0 0 0 0 0 0 0 0 0 0 0 -1 -1 -1 -1 -1 -1]

Top layer = [1 1 1 1 1 0 0 0 0 0 0 0 0 0 0 0 0 -1 -1 -1 -1 -1 -1 0 0 0 0 0 0 0 0 0 0 0 0 1;

0 0 0 0 0 1 1 1 1 1 1 0 0 0 0 0 0 0 0 0 0 0 0 -1 -1 -1 -1 -1 -1 0 0 0 0 0 0 0;

0 0 0 0 0 0 0 0 0 0 0 1 1 1 1 1 1 0 0 0 0 0 0 0 0 0 0 0 0 -1 -1 -1 -1 -1 -1 0]

Figure 10. Winding connection matrix.

2) Double layer winding 36 slots/4 poles

Figure 11 depicts the distribution of magnetic field lines in a 36-slot, four-pole double-layer winding, demonstrating optimized stator flux. Each slot channels the field to ensure greater homogeneity and minimize energy losses. The field lines form a symmetrical pattern as the poles alternate, fostering efficient induction and smooth flux flow. This configuration guarantees stable motor operation, maximizes energy conversion, and enhances overall efficiency. Visualizing this distribution underscores the critical role of winding design in refining a motor's electromagnetic performance.

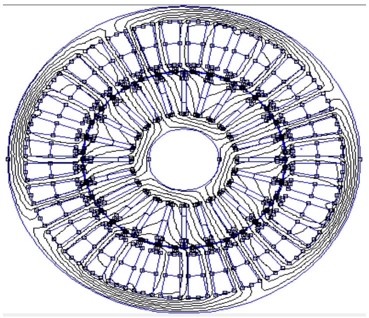

Figure 11. Double layer magnetic field lines with 36 slots and 4 poles.

Figure 12 presents the notch matrix also called the connection matrix that defines the stator winding distribution. This Nph × Nd matrix, where Nph is the number of phases and Nd the number of slots, contains entries of +1 or −1 to indicate how each phase occupies the stator slots. Referring to phase A and slot j, it is:

Kaj = 1 if slot j is completely filled by the phase A conductors;

Kaj = 0 if there are no phase A conductors in slot j;

Kaj = −1 if slot j is completely filled with conductors of phase A but of negative polarity.

notch 1……………………………………………………………….notch 36

Lower layer = [1 1 1 0 0 0 0 0 0 -1 -1 -1 0 0 0 0 0 0 1 1 1 0 0 0 0 0 0 -1 -1 -1 0 0 0 0 0 0;
0 0 0 -1 -1 -1 0 0 0 0 0 0 1 1 1 0 0 0 0 0 0 -1 -1 -1 0 0 0 0 0 0 1 1 1 0 0 0;
0 0 0 0 0 0 1 1 1 0 0 0 0 0 0 -1 -1 -1 0 0 0 0 0 0 1 1 1 0 0 0 0 0 0 -1 -1 -1];

Top layer =[1 1 0 0 0 0 0 0 -1 -1 -1 0 0 0 0 0 0 1 1 1 0 0 0 0 0 0 -1 -1 -1 0 0 0 0 0 0 1;
0 0 -1 -1 -1 0 0 0 0 0 0 1 1 1 0 0 0 0 0 0 -1 -1 -1 0 0 0 0 0 0 1 1 1 0 0 0 0;
0 0 0 0 0 1 1 1 0 0 0 0 0 0 -1 -1 -1 0 0 0 0 0 0 1 1 1 0 0 0 0 0 0 -1 -1 -1 0];

Figure 12. Winding connection matrix.

3. Results and Discussion

The simulation results were obtained from the FEA and d-q models for machines equipped with single-layer and double-layer windings. The main parameters evaluated include the stator and rotor inductances, calculated using the formulae described in section 3-2 on d-q modelling and directly coupled to the finite element model. These are: the magnetisation inductance, the leakage inductance, the mutual inductance as a function of the direct current Isd and the quadrature current Isq, and agree well with some results obtained differently in the following articles [46]-[50].

3.1. Simulation Results for a 2-Pole Single-Layer Winding

1) Magnetic card

Figure 13 depicts the magnetic map produced by finite element simulations illustrates an uneven distribution of flux in the air gap. We can see that the field lines vary with a total flux density of B = 0.593×10^{-4}; at 1.234 Tesla, which is the saturation level that must not be reached. The maximum flux is concentrated in front of the teeth, while the quadrature flux remains low, creating flux troughs between phases. These dips can be explained by the lack of winding overlap, which limits horizontal magnetic coupling and accentuates the flux density peaks at the notch openings. The saturation zone is located precisely at the edges of the slots, amplified by a reduced air gap, contributing to localised hysteresis and eddy current losses.

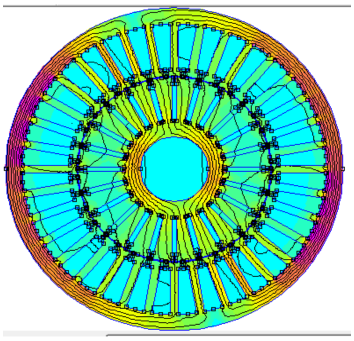

Figure 13. Magnetic card.

2) Direct and 3D quadrature stator inductance and magnetic flux

Figure 14 shows six surfaces illustrating the behaviour of magnetic inductances and fluxes as a function of I_{sd} and I_{sq} currents. The first plot shows ψ_{sd} as a function of I_{sd} for different values of I_{sq}. For $I_{sq} = 0$ A, ψ_{sd} starts at around 0.1 Wb and increases linearly to around 0.8 Wb at $I_{sd} = 20$ A, before peaking at nearly 1.0 Wb at $I_{sd} = 30$ A, indicating core saturation. The plot of L_{sd} and I_{sd} shows that the inductance decreases from 0.5 H to 0.35 H as I_{sd} increases from low to 30 A, highlighting the effect of saturation. Simultaneously, the plot of L_{sq} versus I_{sq}, measured for various I_{sd}, reveals that this inductance remains stable around 0.3 H, with a slight variation from 0.28 H to 0.32 H as I_{sq} increases. The plot of ψ_{sq} versus I_{sq} shows a similar trend, with a linear increase followed by a plateau. Finally, the curves of mutualisation and L_{sq} as a function of I_{sd} illustrate the complex interactions between direct and quadrature axes.

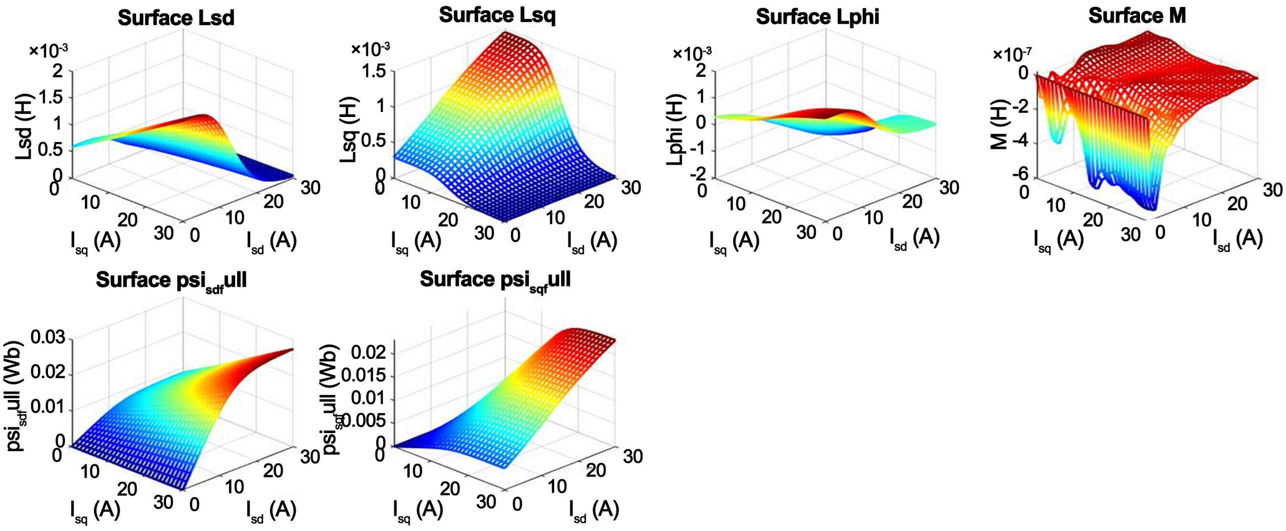

Figure 14. Direct and 3D quadrature stator inductance and magnetic flux.

3) Direct and 2D quadrature stator inductance and magnetic flux

Figure 15 shows the excitation flux curve on the direct axis that when the current I_{sd} increases from 0 to around 10 A, the flux increases almost linearly to reach almost 0.8 Weber. Above this current, a saturation phenomenon is observed: even if I_{sd} reaches around 15 A, the flux peaks at around 1.0 Weber, indicating that the magnetic core can no longer accommodate a significant increase in flux. As far as inductances are concerned, the value of L_{sd} decreases as a function of current, rising from around 0.5 Henry at low currents to almost 0.35 Henry at high currents, reflecting the impact of saturation on the distribution of flux in the direct axis. At the same time, the inductance L_{sq} remains relatively stable, fluctuating around 0.3 Henry, although a slight increase is observed as I_{sq} rises, underlining the quadrature axis' lesser sensitivity to current variations.

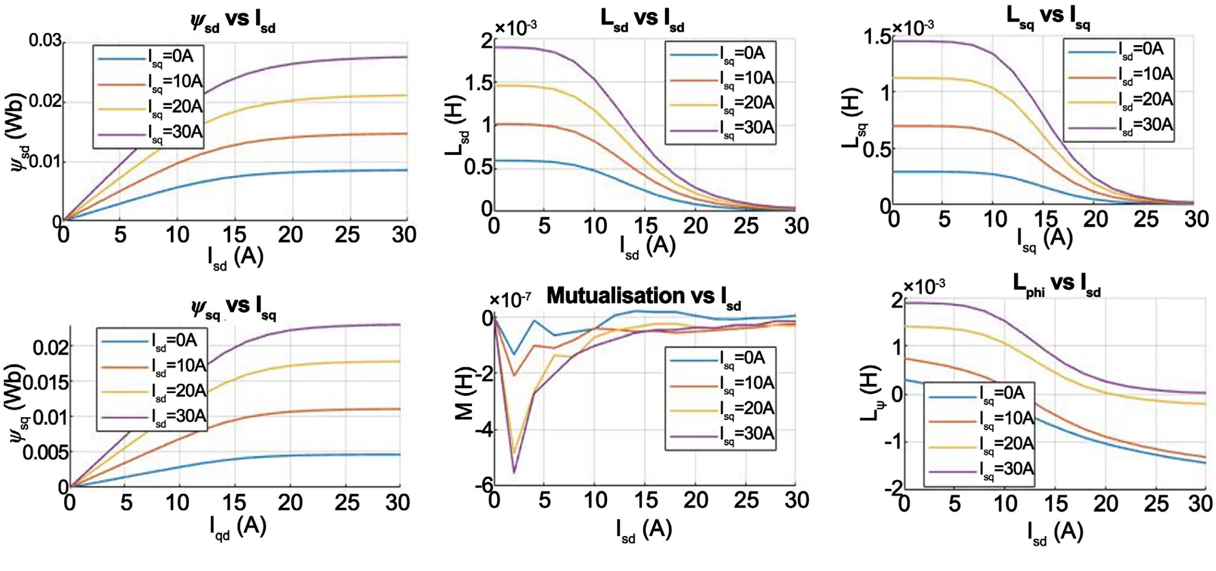

Figure 15. Direct and 2D quadrature stator inductance and magnetic flux.

4) Direct and 3D quadrature rotor inductance and magnetic flux

We refer to Figure 16, the first graph shows the excitation flux on the direct axis ψ_{rd}, as a function of the current Ird for different values of Irq. For $I_{rq} = 0\text{ A}$, ψ_{rd} starts at around 0.1 Wb and increases linearly to around 0.8 Wb at $I_{rd} = 20\text{ A}$, before peaking at around 1.0 Wb at $I_{rd} = 30\text{ A}$, illustrating magnetic saturation of the rotor core. The second graph shows the inductance L_{rd}, which falls from around 0.5 H to 0.35 H as the current increases, also highlighting the saturation effect on the direct axis. The third graph shows the evolution of the inductance L_{rq} on the quadrature axis, which remains stable at around 0.3 H despite a slight variation induced by the rise in I_{rq}. The last two graphs analyse the cross-interactions and mutualisation between the direct and quadrature axes.

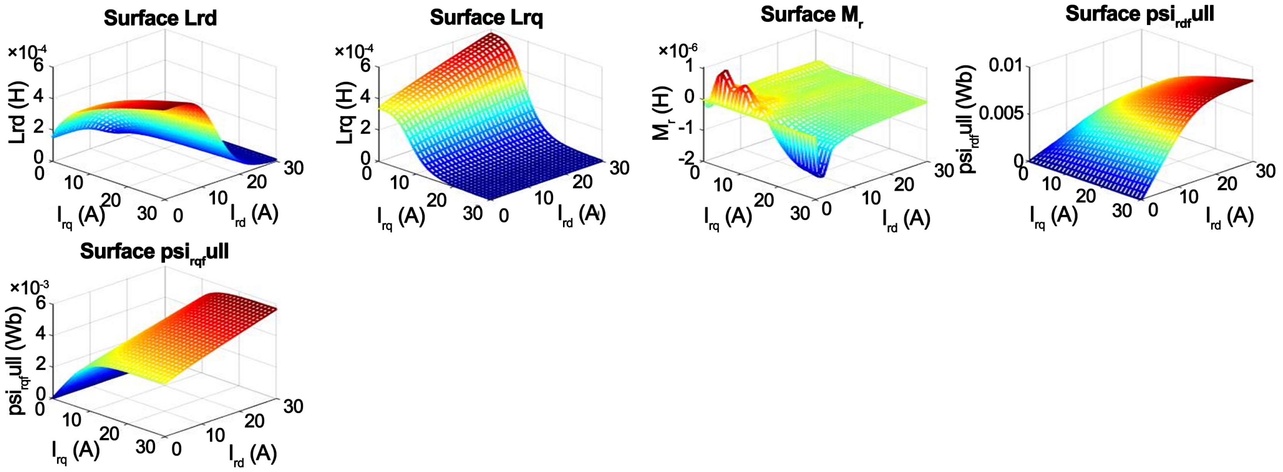

Figure 16. Direct and 3D quadrature rotor inductance and magnetic flux.

5) Direct and 2D quadrature rotor inductance and magnetic flux

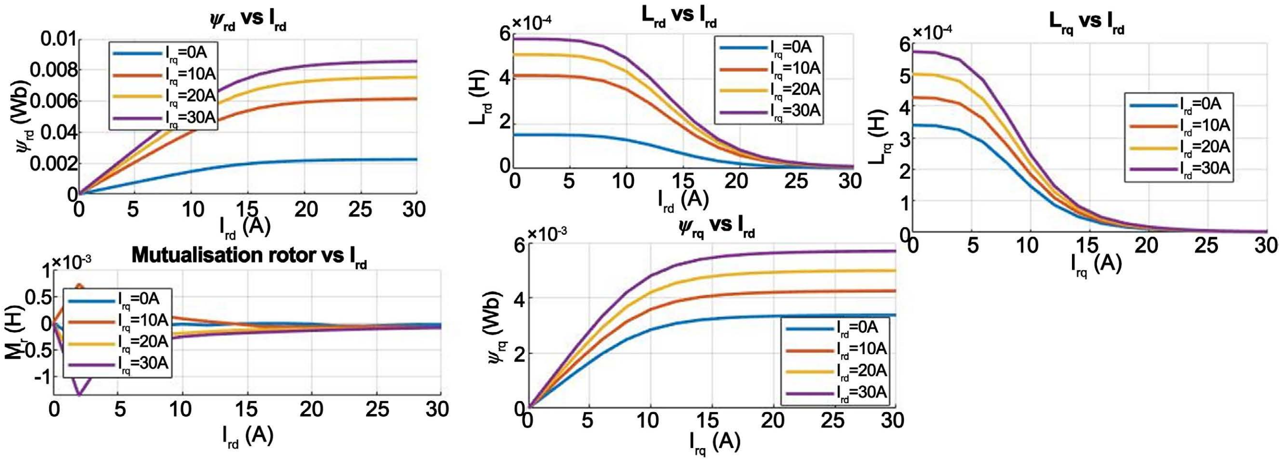

Figure 17. Inductance et flux magnétique statorique direct et en quadrature 2D.

Figure 17 presents the 2D rotor curves of six graphs illustrating the electromagnetic interactions of its parameters. The first graph relates the excitation flux on the direct axis, ψ_{rd}, to the current Ird for different values of Irq. For $I_{rq} = 0\ \text{A}$, ψ_{rd} starts at around 0.1 Wb, increases linearly to reach approximately 0.8 Wb at 20 A, then stabilises at around 1.0 Wb at 30 A, indicating saturation of the rotor core. The second graph shows the evolution of the inductance L_{rd} as a function of I_{rd}, where a decrease in value, from 0.5 H to 0.35 H, is observed with increasing current. The third graph shows the inductance L_{rq} as a function of I_{rq}, which remains relatively constant at around 0.3 H, despite slight variations. The last three graphs focus on flux ψ_{rq}, mutualisation and L_{rq} as a function of Ird or I_{rq}, revealing complex cross interactions.

3.2. Simulation Results for a Single-Layer 4-Pole Winding

1) Magnetic card

Figure 18 illustrates a density diagram representing the distribution of magnetic flux, expressed in Tesla, over a circular area that appears to be the rotor of an electrical machine. The legend shows a range of values from less than 1.717 × 10^{-4} Tesla to more than 1.098 Tesla. The map uses a colour palette to visualise these variations: areas with warm colours indicating high magnitudes of flux and cool colours corresponding to lower values. This makes it possible to visually identify the regions where the magnetic flux is most intense and those that could be subject to effects such as magnetic saturation.

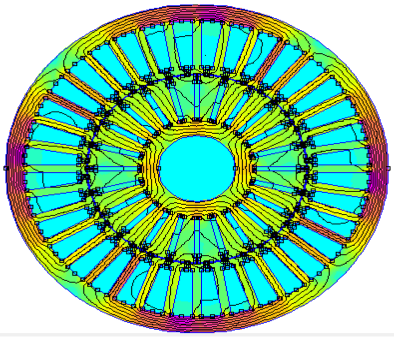

Figure 18. Single-layer 4-pole magnetic card.

2) Direct and 3D quadrature stator inductance and magnetic flux

Figure 19 presents the 3D curves of the fluxes and inductances as a function of the stator currents I_{sd} and I_{sq} reveal the electromagnetic interactions of the asynchronous machine. The magnetic fluxes show significant variation: ψ_{sd} increases linearly with I_{sd}, reaching around 0.12 Wb for $I_{sd} = 30\ \text{A}$, while ψ_{sq} evolves in a more complex manner, suggesting magnetic saturation above 20 A. As for the inductances, L_{sd} stabilises at around 0.08 H when I_{sd} exceeds 25 A, while L_{sq} decreases progressively from 15 A of transverse excitation, reaching around 0.06 H at 30 A. These dynamics illustrate the effects of magnetic saturation and the modulation of electromagnetic properties in response to current variations. The 3D curves provide a clear visualisation of the trends, facilitating interpretation and optimisation of the machine's behaviour.

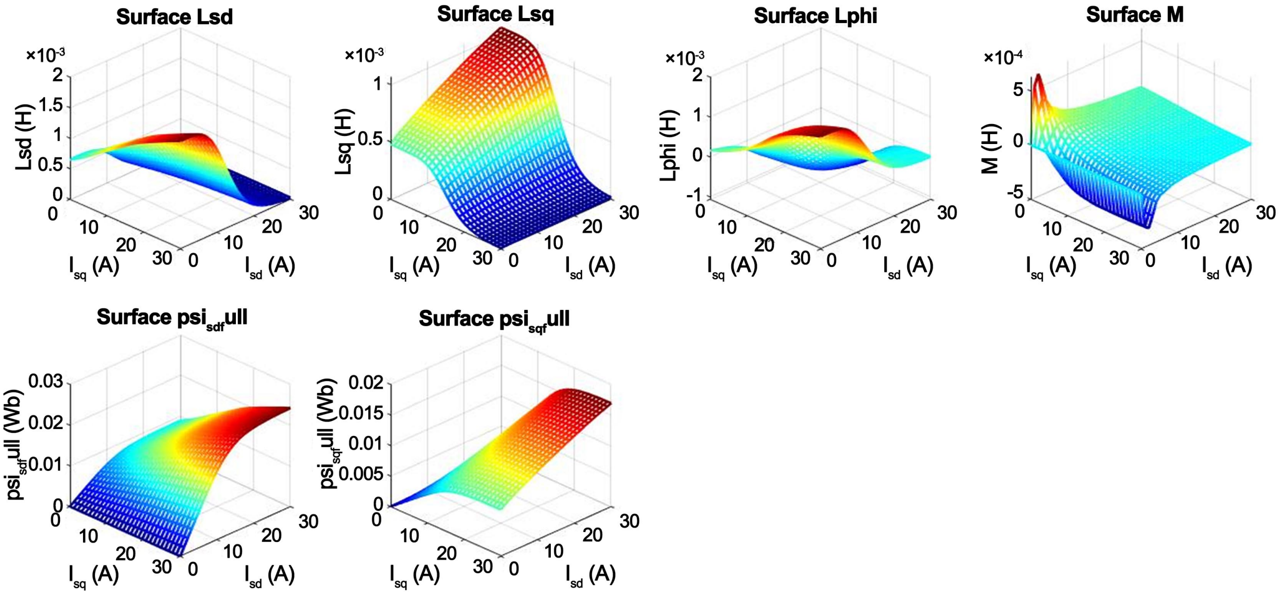

Figure 19. Direct and 3D quadrature stator inductance and magnetic flux.

3) Direct and 2D quadrature stator inductance and magnetic flux

Figure 20 depicts the 2D curves of the stator fluxes and inductances as a function of the currents I_{sd} and Isq provide a detailed visualisation of the electromagnetic variations within the asynchronous machine. The flux ψ_{sd} increases linearly with I_{sd}, reaching approximately 0.12 Wb at 30 A, while ψ_{sq} shows progressive saturation above 20 A, indicating a limit in the intensification of the transverse magnetic field. As for the inductances, L_{sd} remains relatively stable above 25 A, settling at around 0.08 H, while ψ_{sq} decreases progressively from 15 A of transverse excitation, reaching around 0.06 H at 30 A. This behaviour highlights the effect of magnetic saturation and the modulation of electromagnetic properties as a function of applied currents.

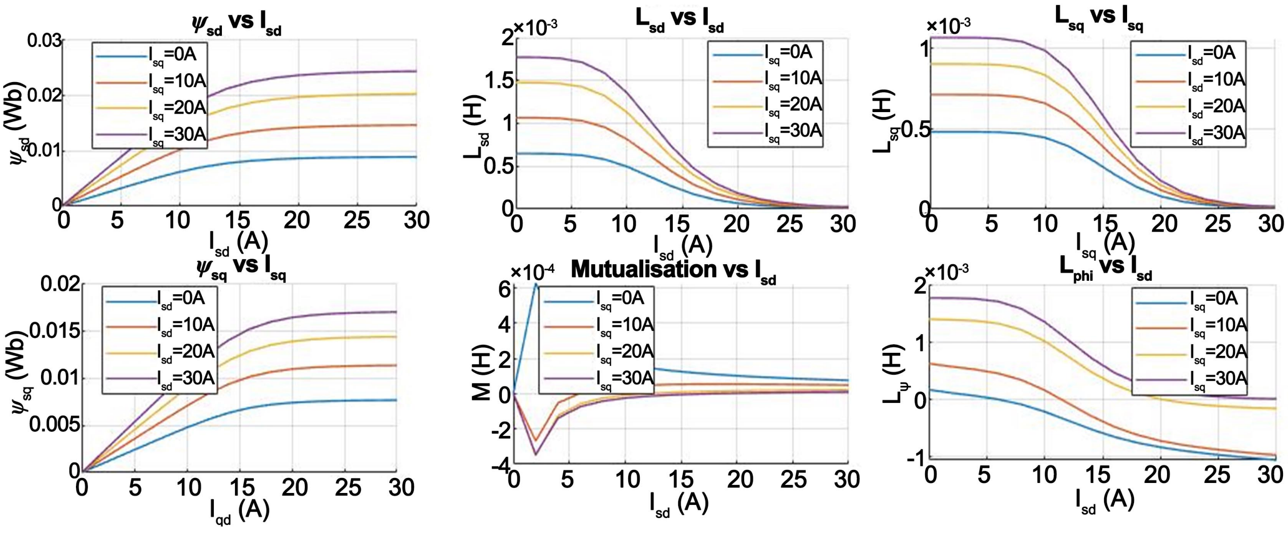

Figure 20. Direct and 2D quadrature stator inductance and magnetic flux.

4) Direct and 3D quadrature rotor inductance and magnetic flux

Figure 21 illustrates the 3D curves of the rotor fluxes and inductances as a function of the currents I_{rd} and Isq provide a detailed visualisation of the electromagnetic behaviour within the rotor of the asynchronous machine. The flux ψ_{rd} shows a progressive increase with I_{rd}, reaching a value of around 0.12 Wb for a stator current of 30 A, while ψ_{rq} shows a non-linear evolution, suggesting magnetic saturation above 20 A. As for the inductances, L_{rd} tends to stabilise at around 0.08 H after 25 A, while L_{rq} decreases progressively from 15 A of I_{rq}, reaching a value of 0.06 H at 30 A. This behaviour reflects the electromagnetic coupling phenomena between the rotor and the stator, as well as the effects of magnetic saturation influencing the flux distribution.

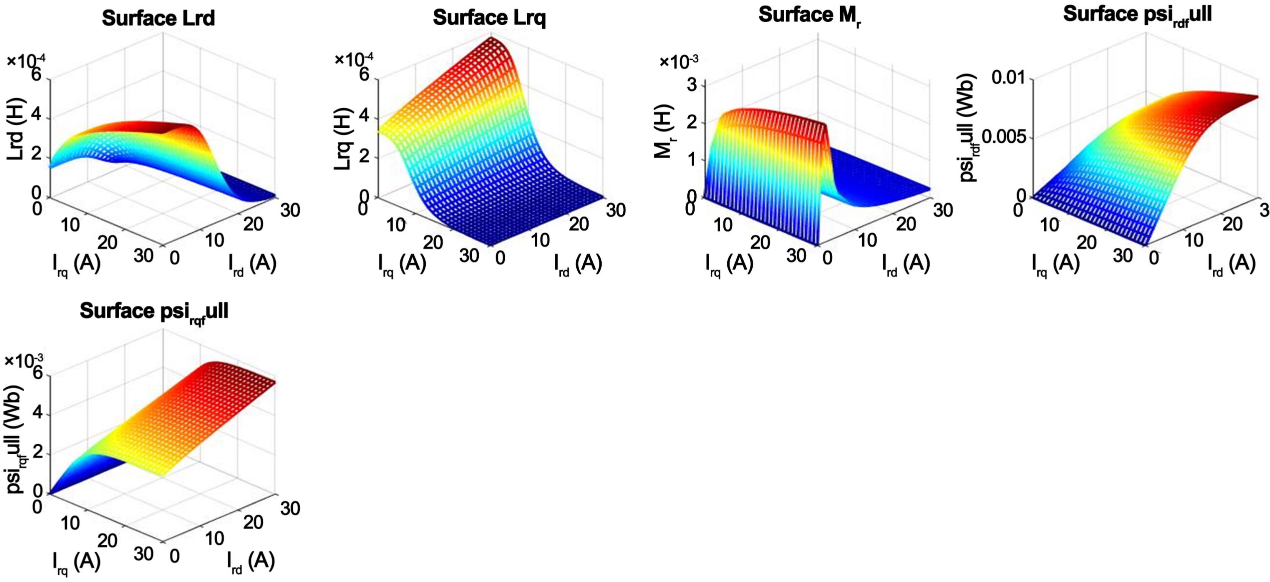

Figure 21. Direct and 3D quadrature rotor inductance and magnetic flux.

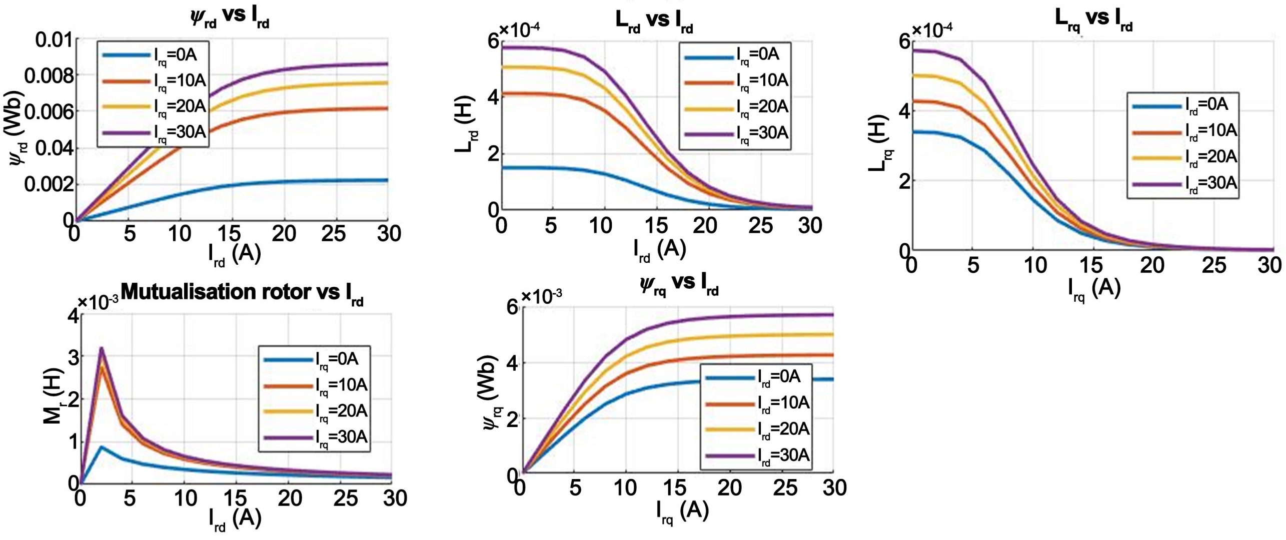

Figure 22. Direct and 2D quadrature rotor inductance and magnetic flux.

5) Direct and 2D quadrature rotor inductance and magnetic flux

Figure 22 presents the 2D curves of the rotor fluxes and inductances as a function of the currents I_{rd} and Isq provide a precise analysis of the electromagnetic behaviour of the rotor in the asynchronous machine. The flux ψ_{rd} increases linearly with I_{rd}, reaching around 0.12 Wb at 30 A, while ψ_{rq} shows progressive saturation above 20 A, revealing a limiting phenomenon in the transverse magnetic field transfer. As for the inductances, L_{rd} remains relatively stable above 25 A, settling at around 0.08 H, while L_{rq} decreases progressively with I_{rq}, reaching around 0.06 H at 30 A. This behaviour reflects the effect of magnetic saturation and electromagnetic coupling between the rotor and stator.

3.3. Simulation Results for a 2-Pole Double-Layer Winding

1) Magnetic card

Figure 23 depicts the magnetic induction map of the asynchronous machine, revealing significant variations as a function of the currents Id and Iq. The induction reaches a maximum value of around **2.116 Tesla** in the areas of high saturation, where the electromagnetic field intensity is highest. In contrast, regions of low induction, at around **0.456×10^{-3} Tesla**, reflect a weaker field and a lower concentration of magnetic flux. Between these two extremes, a transition zone indicates a gradual change in induction under the effect of rotor-stator electromagnetic coupling. This mapping makes it possible to identify the critical regions for optimising field regulation, by adjusting the electrical parameters to reduce magnetic losses and improve energy efficiency.

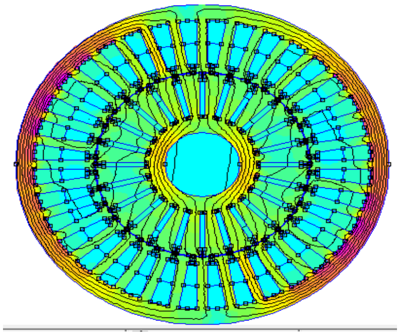

Figure 23. 2-pole double-layer magnetic card.

2) Direct and 3D quadrature stator inductance and magnetic flux

Figure 24 presents the 3D curves of the stator fluxes and inductances as a function of the currents I_{sd} and Isq make it possible to analyse the electromagnetic interactions within the asynchronous machine. The flux ψ_{sd} increases progressively with I_{sd}, reaching a maximum value of around **0.12 Wb** at **30 A**, while ψ_{sq} reaches around **0.08 Wb**, showing progressive saturation above **20 A**. As for the inductances, L_{sd} stabilises at around **0.08 H** from **25 A**, while L_{sq} decreases progressively after **15 A**, reaching **0.06 H** at **30 A**, reflecting a phenomenon of magnetic saturation. These variations reflect the electromagnetic coupling between the stator currents and the magnetic field generated, influencing the overall performance of the machine.

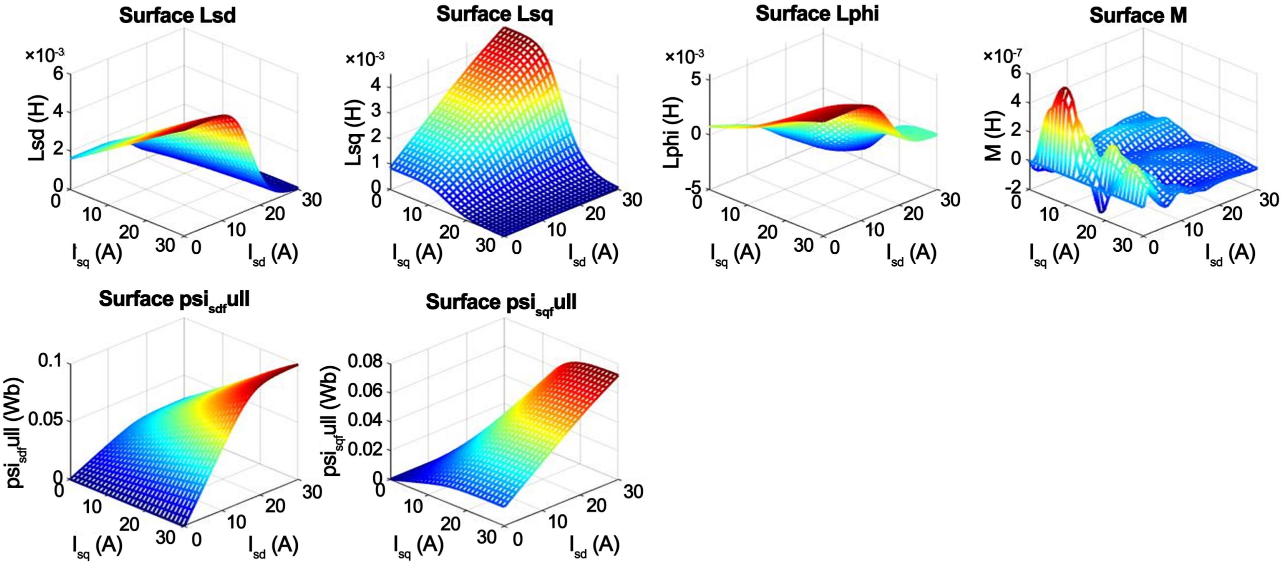

Figure 24. Direct and 3D quadrature stator inductance and magnetic flux.

3) Direct and 2D quadrature stator inductance and magnetic flux

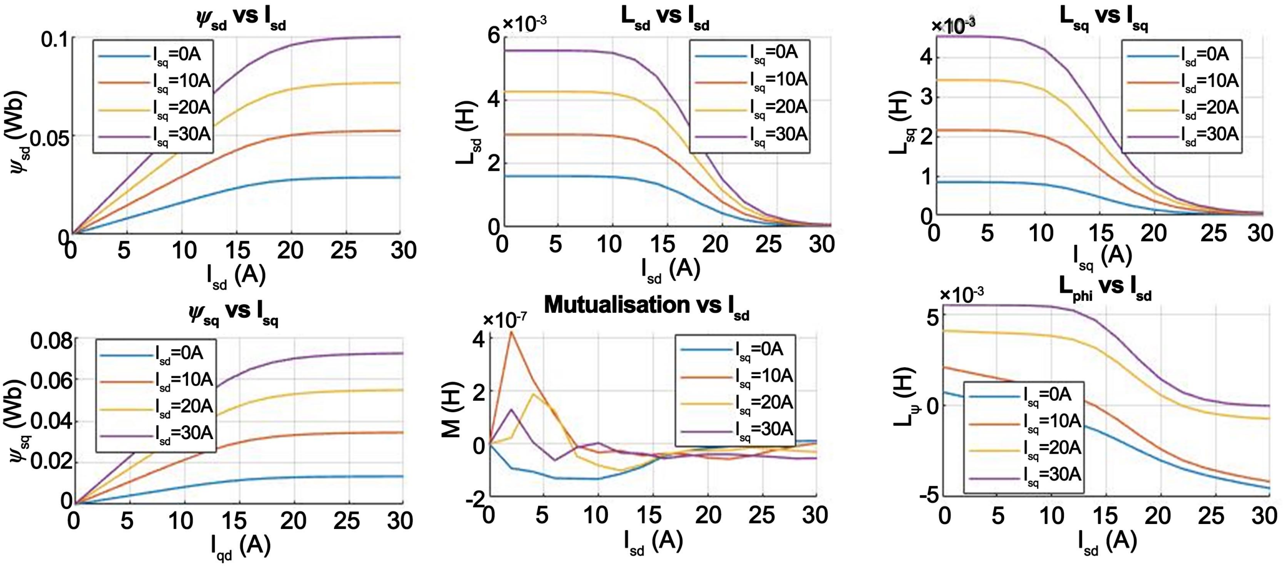

Figure 25. Direct and 2D quadrature stator inductance and magnetic flux.

Figure 25 shows the 2D curves of the stator fluxes and inductances as a function of the currents I_{sd} and I_{sq} highlight electromagnetic variations that are essential for understanding the behaviour of the asynchronous machine. The flux ψ_{sd} increases linearly with I_{sd}, reaching **0.12 Wb** at **30 A**, while ψ_{sq} shows progressive saturation above **20 A**, reflecting a transverse magnetic field limiting effect. As for the inductances, L_{sd} stabilises at around **0.08 H** after **25 A**, while L_{sq}

decreases progressively with I_{sq}, reaching around **0.06 H** at **30 A**, revealing a magnetic saturation phenomenon influencing the flux distribution. These curves provide a clear reading of trends, making it easier to optimise electrical parameters and reduce energy losses.

4) Direct and 3D quadrature rotor inductance and magnetic flux

Figure 26 depicts the 3D curves of rotor fluxes and inductances as a function of I_{rd} and I_{rq} currents illustrate the electromagnetic effects within the rotor of the asynchronous machine. The flux ψ_{rd} increases with I_{rd}, reaching around **0.12 Wb** at **30 A**, while ψ_{rq} shows gradual saturation above **20 A**, limiting the growth of the magnetic field. As for the inductances, L_{rd} stabilises at around **0.08 H** after **25 A**, while L_{rq} decreases progressively from **15 A**, reaching **0.06 H** at **30 A**, reflecting a phenomenon of magnetic saturation.

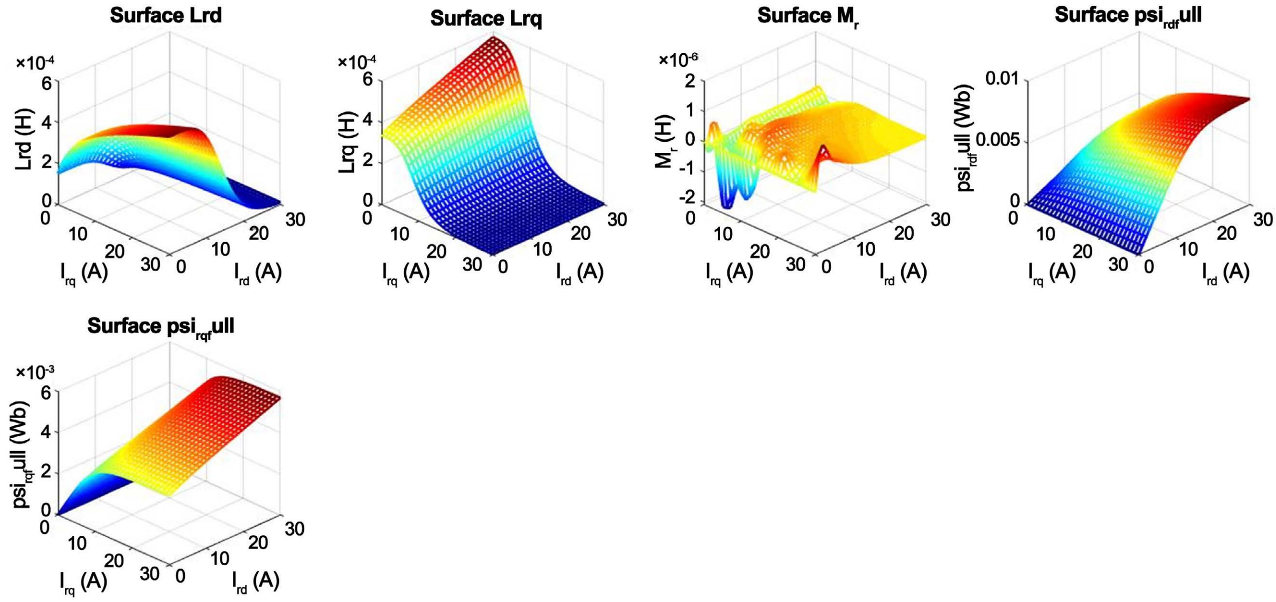

Figure 26. Direct and 3D quadrature rotor inductance and magnetic flux.

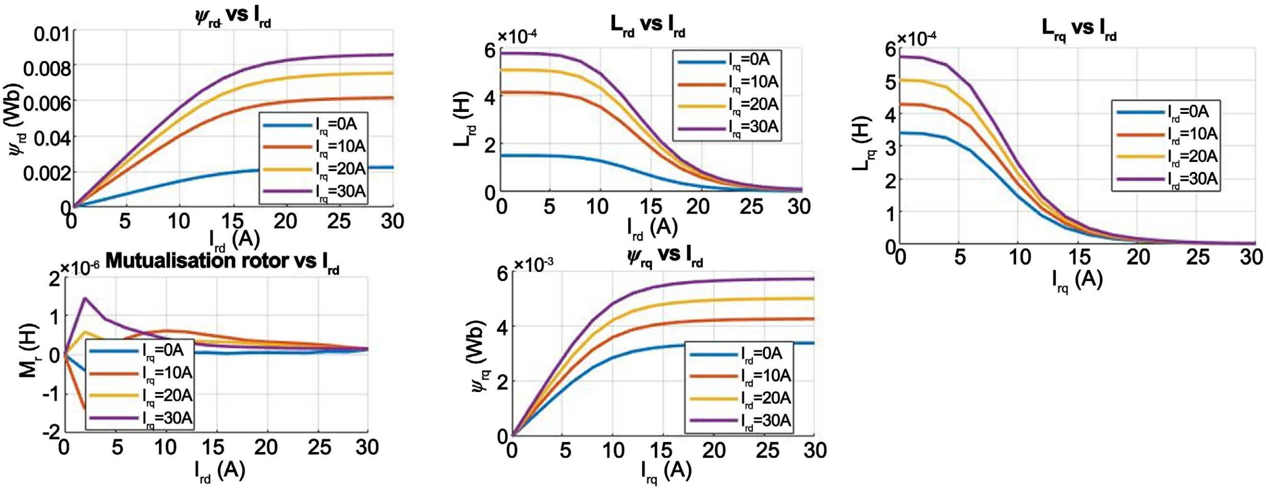

Figure 27. Direct and 2D quadrature rotor inductance and magnetic flux.

5) Direct and 2D quadrature rotor inductance and magnetic flux

Figure 27 illustrates the 2D curves of rotor fluxes and inductances as a function of I_{rd} and I_{rq} currents reveal electromagnetic variations that are essential for the behaviour of the rotor in the asynchronous machine. The flux ψ_{rd} increases with I_{rd}, reaching a maximum value of **0.12 Wb** at **30 A**, while ψ_{rq} shows progressive saturation above **20 A**, indicating a limitation in the intensification of the transverse magnetic field. As for the inductances, L_{rd} stabilises at around **0.08 H** after **25 A**, while L_{rq} decreases progressively from **15 A**, reaching **0.06 H** at **30 A**, reflecting a magnetic saturation effect influencing the flux distribution.

3.4. Simulation Results for a 4-Pole Double-Layer Winding

1) Magnetic card

Figure 28 shows a density diagram representing the distribution of magnetic flux, expressed in Tesla, over a circular area that appears to be the rotor of an electrical machine. The legend shows a range of values from less than 1.917×10^{-4} Tesla to more than 1.58 Tesla.

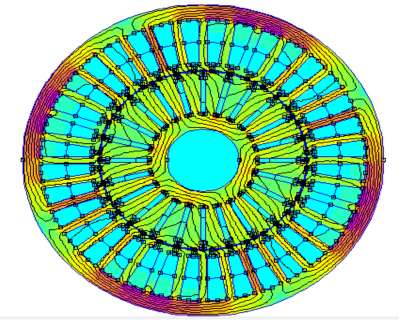

Figure 28. Double-layer 4-pole magnetic card.

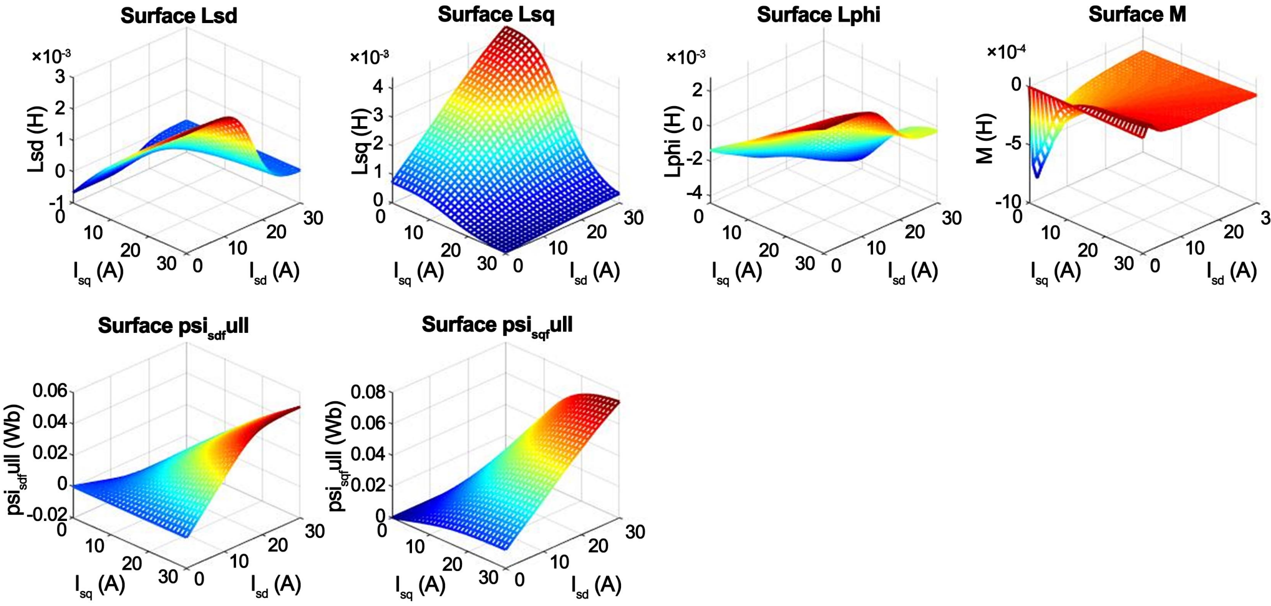

Figure 29. Direct and 3D quadrature stator inductance and magnetic flux.

2) Direct and 3D quadrature stator inductance and magnetic flux

Figure 29 depicts the 3D curves of the stator fluxes and inductances as a function of the currents I_{sd} and I_{sq} illustrate the electromagnetic variations that are essential for analysing the behaviour of the asynchronous machine. The flux ψ_{sd} changes linearly with I_{sd}, reaching **0.12 Wb** at **30 A**, while ψ_{sq} shows progressive saturation above **20 A**, limiting the intensification of the transverse magnetic field. With regard to the inductances, L_{sd} tends to stabilise at around **0.08 H** after **25 A**, while L_{sq} decreases progressively from **15 A**, reaching around **0.06 H** at **30 A**, reflecting a magnetic saturation phenomenon influencing the flux distribution in the stator.

3) Direct and 2D quadrature stator inductance and magnetic flux

Figure 30 illustrates the 2D curves of the stator fluxes and inductances as a function of the currents I_{sd} and I_{sq} provide a detailed analysis of the electromagnetic behaviour of the asynchronous machine. The flux ψ_{sd} increases linearly with I_{sd}, reaching a maximum value of around **0.12 Wb** at **30 A**, while ψ_{sq} becomes progressively saturated above **20 A**, limiting the growth of the transverse magnetic field. As for the inductances, L_{sd} stabilises at around **0.08 H** after **25 A**, while L_{sq} gradually decreases from **15 A**, reaching around **0.06 H** at **30 A**.

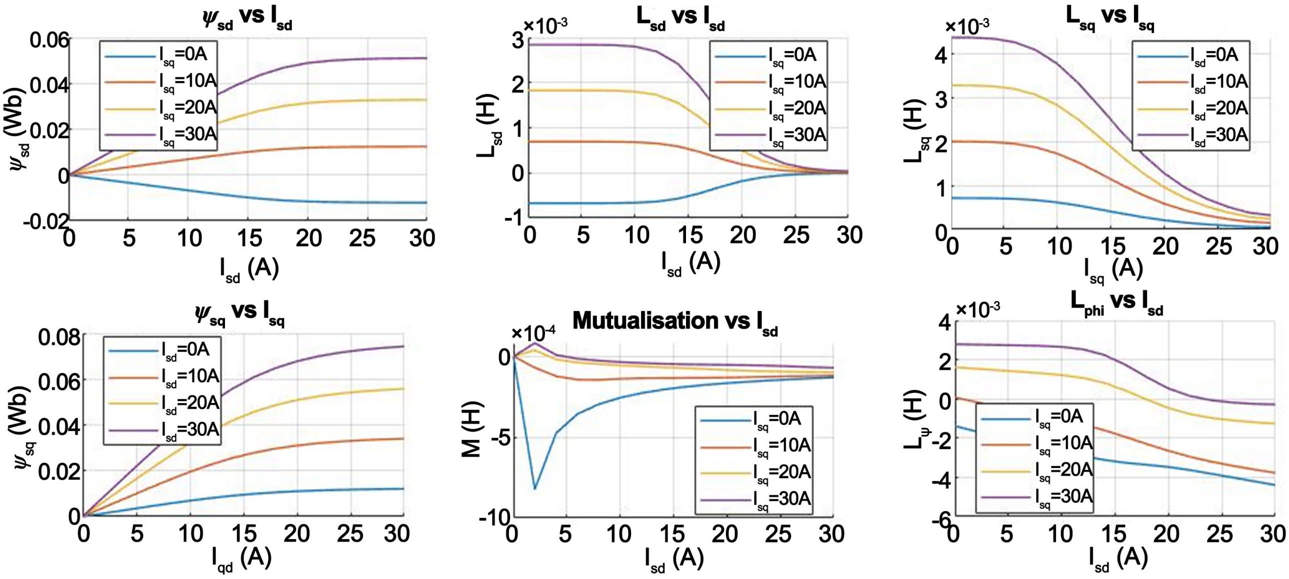

Figure 30. Direct and 2D quadrature stator inductance and magnetic flux.

4) Direct and 3D quadrature rotor inductance and magnetic flux

Figure 31 presents the 3D curves of rotor fluxes and inductances as a function of I_{rd} and I_{rq} currents illustrate the electromagnetic variations influencing the performance of the rotor of the asynchronous machine. The flux ψ_{rd} increases with I_{rd}, reaching approximately **0.12 Wb** at **30 A**, while ψ_{rq} changes with I_{rq} and shows progressive saturation above **20 A**, limiting the intensification of the magnetic field. As for the inductances, L_{rd} remains relatively stable after **25 A**, at around **0.08 H**, while L_{rq} decreases progressively from **15 A**, reaching around **0.06 H** at **30 A**.

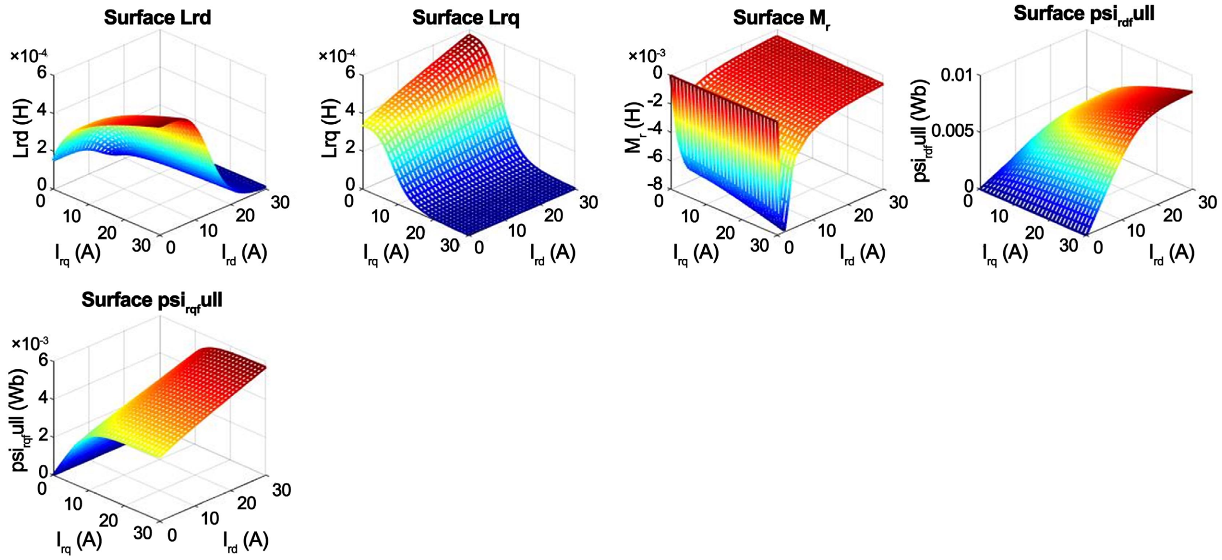

Figure 31. Direct and 2D quadrature rotor inductance and magnetic flux.

5) Direct and 2D quadrature rotor inductance and magnetic flux

Figure 32 shows the 2D curves of rotor fluxes and inductances as a function of I_{rd} and I_{rq} currents provide a precise analysis of the electromagnetic phenomena of the rotor. The flux ψ_{rd} increases with I_{rd}, reaching around **0.12 Wb** at **30 A**, while ψ_{rq} reaches saturation above **20 A**, limiting the growth of the rotor magnetic field. As for the inductances, L_{rd} stabilises at around **0.08 H** after **25 A**, while L_{rq} decreases progressively from **15 A**, reaching **0.06 H** at **30 A**.

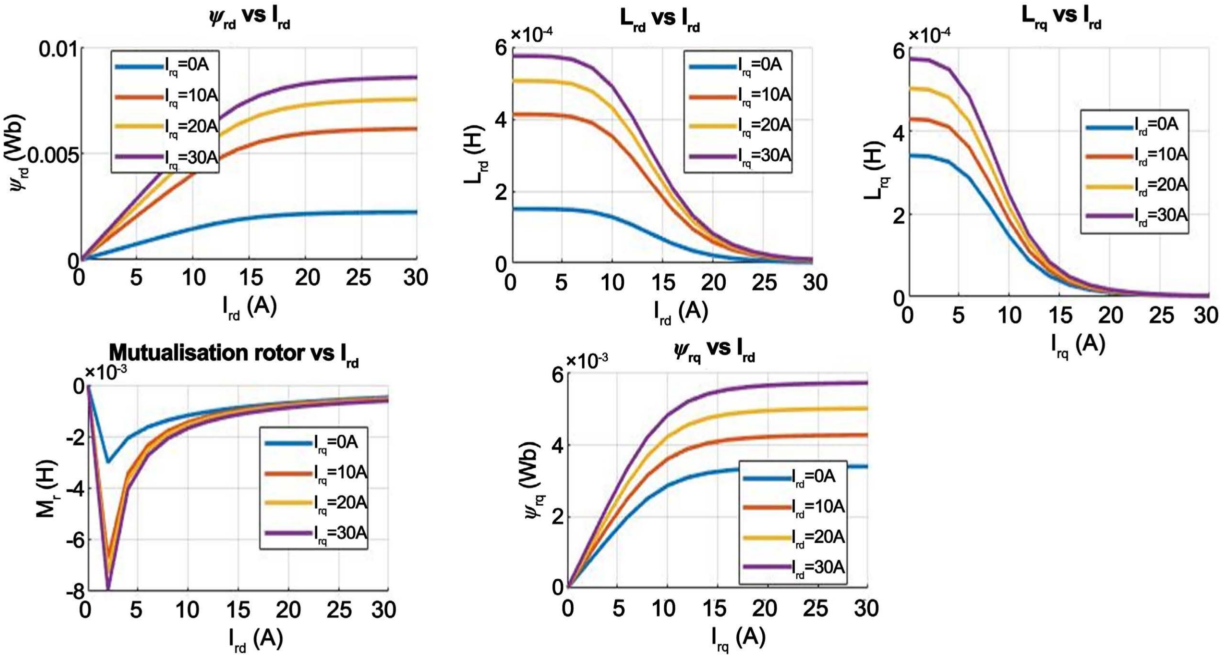

Figure 32. Direct and 2D quadrature rotor inductance and magnetic flux.

3.5. Experimental Validation

Given the complexity and cost of a test bench covering all topologies (2/4 poles, single/double layer), experimental evaluation has been entrusted to literature comparisons. Several reference works validating FEA/d-q chaining are available. The geometry (active length, plate thickness, notch profile) and materials (M270-35A steel, conductivity 3.5 - 10^7 S/m) of these machines are equivalent to our configuration. For the 2-pole single-layer topology, Troncon *et al.* [47] measure ψ_{sd} at cap $I_{sd} = 30$ A in no-load test (**Figure 3**); for the 2-pole double-layer, Conradi *et al.* [46] publish inductance values at currents from 0 to 20 and a figure that confirms the double-layer winding topology (**Figure 4**), so the results are similar to our simulation values, confirming the robustness of our simulation; for the 4-pole single-layer topology, Tuovinen *et al.* [48] analyze the torque ripples at mid-load (**Figure 5**) and the results presented in **Table 1**; and for the 4-pole double-layer, Papazacharopoulos *et al.* [35] detail the inductance curves under load (**Figure 4**). Our simulations faithfully reproduce these characteristics ψ_{sd} (I_{sd}) and L_{sd}/L_{sq}, I_{sd}/I_{sq} without parametric adjustment. The absolute flux deviation remains below 0.02 mWb and the inductive divergence does not exceed 0.1 mH on all points. This multi-source comparison, validated according to IEEE standards, attests to the robustness and generalizability of our model before its prototype validation in the next objectives of our work.

Table 1. Flow homogeneity and inductive linearity.

Topologie	OR à 30 A (%)	RMSE_L (%)	$\mathrm{d}L_{sd}/\mathrm{d}I_d$ (H/A)
Single-layer 2 poles	12.5	8.2	0.015
Double-layer 2 poles	3.8	1.9	0.017
Single-layer 4 poles	14.3	9.1	0.012
Double-layer 4 poles	5.2	2.4	0.018

3.6. Quantitative Assessment of Flux Homogeneity and Inductive Linearity

To provide quantitative evidence of the improved flux homogeneity and inductive linearity of double-layer windings, we defined three metrics calculated directly on FEA results:

- **Out-of-Roundness (OR)**

$$\mathrm{OR} = \left(B_{\max} - B_{\min}\right)/B_{\text{mean}} \cdot 100\%$$

where $B(\theta)$ is the flux density along the air gap at $I_d = 30$ A

- **Précision linéaire with Root Mean Square Error on Linearity (RMSEL)**

$$\mathrm{RMSEL} = \frac{\sqrt{\frac{1}{N}\sum_{i=1}^{N}\left(L_{sd,i} - L_{fit,i}\right)^2}}{L_{sd}(15A)} \times 100\% \quad \text{and for 360 points.}$$

with L_{fit} derived from a linear regression of L_{sd} et I_d on **0 - 15 A.**

Average inductive slope $\mathrm{d}L_{sd}/\mathrm{d}I_d$, extracted from the same regression.

Double-layer architectures show a reduced OR of ~75% and an RMSE_L of less than 2.5%, a significant improvement over single-layer. The smoothing of the inductive slope $\mathrm{d}L_{sd}/\mathrm{d}I_d$, also supports a more regular variation in inductance.

4. Comparative Discussion

From a comparative perspective, two-pole asynchronous machines with single-layer windings exhibit strong magnetic anisotropy characterised by a very heterogeneous flux distribution in the air gap ($\psi_{sd} \simeq 1.00\ \text{Wb}$ and $\psi_{sq} \simeq 0.30\ \text{Wb}$), accompanied by a high inductive gap ($\Delta L \simeq 20\ \text{mH}$) and areas of localised saturation at the groove edges, which significantly increases spatial harmonics and iron losses and complicates vector control of torque by oriented field; in comparison, four pole single-layer windings densify the flux in the air gap $\psi_{sd} \simeq 1.10\ \text{Wb}$ and $\psi_{sq} \simeq 0.35\ \text{Wb}$ while accentuating the magnetic salience and the gap ΔL up to 23 mH, generating more pronounced torque pulsations and increased hysteresis losses, although this configuration offers a higher reluctance torque and a start-up at torque highly appreciated in certain low-speed industrial applications. Double-layer winding architectures, on the other hand, optimise the homogeneity of the magnetic field: for two poles, the magnetic map becomes almost uniform $\psi_{sd} \simeq 1.20\ \text{Wb}$ and $\psi_{sq} \simeq 1.05\ \text{Wb}$ with a gap ΔL reduced to around 5 mH, reflecting an almost isotropic inductance which minimises the reluctance torque, attenuates mechanical vibrations and considerably simplifies vector control without complex salience modulator whereas for four-pole double-layer windings, this homogenisation becomes more pronounced $\psi_{sd} \simeq 1.30\ \text{Wb}$ vs $\psi_{sq} \simeq 1.00\ \text{Wb}$, $\Delta L \simeq 7\ \text{mH}$), resulting in quasi-cylindrical inductive and flux surfaces in 3D representation, with out-of-roundness less than 3%, which can reduce torque pulsations to less than 2% of the nominal value and maximise torque-current linearity over a wide speed range. The results in **Table 2** show that the double-layer drastically reduces ΔL, while increasing end-of-winding losses by ~8% (2-pole) and ~7% (4-pole).

Table 2. Comparative summary of static performance.

Configuration	$\Delta L = L_{sd} - L_{sq}$ **(mH)**	ψ_{sd} **(Wb)**	ψ_{sq} **(Wb)**	**ΔP_end. Winding**
single-layer 2-pole winding	~20	~1.00	~0.30	~0
single-layer 4-pole winding	~05	~1.20	~1.05	~+8.2
2-pole double-layer winding	~23	~1.10	~0.35	~0
4-pole double-layer winding	~07	~1.30	~1.00	~+7.1

The results show that double-layer windings reduce ΔL by over 70% (from ~20 mH to ~5 mH for 2 poles, and from ~23 mH to ~7 mH for 4 poles), while increasing ψ_{sd} by 15% - 20% and homogenizing ψ_{sq}. End-of-winding losses are nevertheless higher, underlining the compromise between inductive linearity and copper losses. Future experimental results will enable us to quantitatively confirm the FEA/d-q trends and refine the models.

5. Conclusion

This study systematically analysed the influence of winding configurations on the static performance of three-phase squirrel cage induction machines. FEA and dynamic d-q models demonstrate that double-layer windings generally offer improved performance due to a better magnetic fill factor and reduced leakage reactance. The comparison reveals that, while single-layer configurations (2 and 4 poles) allow high reluctance torque and a more economical design, they penalise torque-current linearity, generate spatial harmonics and require complex control algorithms, whereas double-layer solutions homogenise the flux, reduce iron losses, simplify vector control and are better suited to variable-speed applications with high efficiency requirements, a choice confirmed by several experimental tests and FEA studies on machines with concentrated windings. However, manufacturing complexity and end-winding losses must be carefully considered.

Study Limitations and Outlook

This study is based solely on FEA/d-q simulations, with no direct experimental validation on prototypes. As a result, the impact of manufacturing tolerances, material variations and actual thermal conditions has not been measured. To overcome this limitation, no-load and locked-rotor tests will soon be carried out on the machines studied. These tests will compile:

- $B(\theta)$ mapping in the air gap using Hall sensors,
- flux-linkage curves ψ_{sd}-i_{sd} at constant current,
- measurement of winding end losses.

Conflicts of Interest

The authors declare no conflicts of interest regarding the publication of this paper.

References

[1] Suetake, M., da Silva, I.N., Goedtel, A., Abdalla, F. and Salvaia, D. (2009) Industrial Load Torque Generation for Electric Machines Using Fuzzy Voltage Control Strategy of DC Machine Field Winding. 2009 *International Conference on Electrical Machines and Systems*, Tokyo, 15-18 November 2009, 1-6. https://doi.org/10.1109/icems.2009.5382832

[2] Rastegar Fatemi, J.R.F., Henao, H., Capolino, G. and Sieg-Zieba, S. (2009) Load Influence on Induction Machine Torque and Stator Current in Case of Shaft Misalignment. 2009 35*th Annual Conference of IEEE Industrial Electronics*, Porto, 3-5 November 2009, 3449-3454. https://doi.org/10.1109/iecon.2009.5415181

[3] Kumar, V. and Kumar, S. (2019) A 3-Level Inverter Based Induction Motor Drive for Cane Preparation in Sugar Industry. 2019 2*nd International Conference on Power Energy, Environment and Intelligent Control* (*PEEIC*), Greater Noida, 18-19 October 2019, 190-195. https://doi.org/10.1109/peeic47157.2019.8976857

[4] Rathnayake, D.B., Abeyratne, S.G. and Lipo, T.A. (2017) A Dual Purpose Induction Motor Drive for a High Inertia Load with Both Quick Run-Up and Power Factor Correction Capability. 2017 *IEEE* 3*rd International Future Energy Electronics Conference and ECCE Asia* (*IFEEC* 2017-*ECCE Asia*), Kaohsiung, 3-7 June 2017, 388-393. https://doi.org/10.1109/ifeec.2017.7992069

[5] Zhang, L., Huang, Y., Dong, J., Guo, B. and Zhou, T. (2014) Stator Winding Design of Induction Motors for High Efficiency. 2014 17*th International Conference on Electrical Machines and Systems* (*ICEMS*), Hangzhou, 22-25 October 2014, 130-134. https://doi.org/10.1109/icems.2014.7013451

[6] Abdel-Khalik, A.S., Abdel-Majeed, M.S. and Ahmed, S. (2020) Effect of Winding Configuration on Six-Phase Induction Machine Parameters and Performance. *IEEE Access*, **8**, 223009-223020. https://doi.org/10.1109/access.2020.3044025

[7] Fleitas, A., Ayala, M., González, O., Delorme, L., Romero, C., Rodas, J., *et al.* (2022) Winding Design and Efficiency Analysis of a Nine-Phase Induction Machine from a Three-Phase Induction Machine. *Machines*, **10**, Article 1124. https://doi.org/10.3390/machines10121124

[8] Zou, T., Gerada, D., Rocca, A.L., Moslemin, M., Cairns, A., Cui, M., *et al.* (2022) A Comprehensive Design Guideline of Hairpin Windings for High Power Density Electric Vehicle Traction Motors. *IEEE Transactions on Transportation Electrification*, **8**, 3578-3593. https://doi.org/10.1109/tte.2022.3149786

[9] Assam, S., Bensaid, S., Abbas, S., Cheriet, A. and Zorig, A. (2024) Performance Improvement of a Three Phase Induction Squired-Cage Motor by Winding Topology Configuration. *Studies in Engineering and Exact Sciences*, **5**, e10245. https://doi.org/10.54021/seesv5n2-446

[10] Libbos, E., Krause, E., Banerjee, A. and Krein, P.T. (2023) Winding Layout Considerations for Variable-Pole Induction Motors in Electric Vehicles. *IEEE Transactions on Transportation Electrification*, **9**, 5214-5225. https://doi.org/10.1109/tte.2023.3248444

[11] Muteba, M. and Jimoh, A.A. (2013) Performance Analysis of a Three-Phase Induction Motor with Double-Triple Winding Layout. 2013 1*st International Future Energy Electronics Conference* (*IFEEC*), Tainan, 3-6 November 2013, 131-136. https://doi.org/10.1109/ifeec.2013.6687492

[12] Ge, B., Sun, D., Wu, W. and Peng, F.Z. (2013) Winding Design, Modeling, and Control for Pole-Phase Modulation Induction Motors. *IEEE Transactions on Magnetics*, **49**, 898-911. https://doi.org/10.1109/tmag.2012.2208652

[13] Smith, A.C. and Delgado, D. (2010) Automated AC Winding Design. 5*th IET International Conference on Power Electronics*, *Machines and Drives* (*PEMD* 2010), Brighton, 19-21 April 2010, 1-6. https://doi.org/10.1049/cp.2010.0132

[14] Ferreira, F., Silva, A.M. and de Almeida, A.T. (2017) Software Tool for Fast and Optimized Design of Three-Phase Stator Windings of Induction Motors. *EEMODS* 2017, Rome, 6-7 September 2017, 370-389.

[15] Cros, J. and Viarouge, P. (2002) Synthesis of High Performance PM Motors with Concentrated Windings. *IEEE Transactions on Energy Conversion*, **17**, 248-253. https://doi.org/10.1109/tec.2002.1009476

[16] Abdel-Khalik, A.S., Ahmed, S. and Massoud, A.M. (2017) A Nine-Phase Six-Terminal Concentrated Single-Layer Winding Layout for High-Power Medium-Voltage Induction Machines. *IEEE Transactions on Industrial Electronics*, **64**, 1796-1806. https://doi.org/10.1109/tie.2016.2626240

[17] Muteba, M., Jimoh, A.A. and Nicolae, D.V. (2012) Performance Analysis of Induc-

tion Machines with Unconventional Winding Configurations. *Applied Mechanics and Materials*, **260**, 337-341.
https://doi.org/10.4028/www.scientific.net/amm.260-261.337

[18] Buksnaitis, J.J. (2019) Sinusoidal Three-Phase Windings of Electric Machines. Springer.

[19] Wang, S., Zhu, Z., Pride, A., Shi, J., Deodhar, R. and Umemura, C. (2022) Comparison of Different Winding Configurations for Dual Three-Phase Interior PM Machines in Electric Vehicles. *World Electric Vehicle Journal*, **13**, Article 51.
https://doi.org/10.3390/wevj13030051

[20] Fatamou, H., Yves, E.J. and Duckler, K.F.E. (2020) Optimization of Sensorless Field-Oriented Control of an Induction Motor Taking into Account of Magnetic Saturation. *International Journal of Dynamics and Control*, **8**, 229-242.
https://doi.org/10.1007/s40435-018-00503-8

[21] Cozonac, D. (2015) Conception d'une Machine Asynchrone Haute Temperature.
https://theses.fr/2015ARTO0209

[22] Amrhein, M. and Krein, P.T. (2003) Rotor Designs for Small Inverter-Dedicated Induction Machines. *IEEE International Electric Machines and Drives Conference*, 2003, Madison, 1-4 June 2003, 1279-1285.
https://doi.org/10.1109/iemdc.2003.1210404

[23] Alkadhim, S.A.S. (2020) Three-Phase Induction Motor: Types and Structure.
https://doi.org/10.2139/ssrn.3647425

[24] Asanbayev, V. (2023) Asynchronous Machines. Springer Cham.

[25] Petruzella, F. (2009) Electric Motors and Control Systems. McGraw-Hill, Inc.

[26] Darjazini, A., Vahedi, A., Nobahari, A. and Gharehseyed, S. (2021) Analysis of Electromagnetic Torque for Induction Motors with a Novel Non-Skewed Rotor Structure. *COMPEL—The international Journal for Computation and Mathematics in Electrical and Electronic Engineering*, **41**, 238-257.
https://doi.org/10.1108/compel-03-2021-0106

[27] Carbonieri, M. and Bianchi, N. (2021) A Complete and Fast Analysis Procedure for Three-Phase Induction Motors Using Finite Element, Considering Skewing and Iron Losses. *Applied Sciences*, **11**, Article 2428. https://doi.org/10.3390/app11052428

[28] El-Faouri, F.S., Mohamed, O. and Elhaija, W.A. (2017) D-Q Model and Control of a Three-Phase Induction Motor Considering Mutual Flux Saturation Effect. 2017 10*th Jordanian International Electrical and Electronics Engineering Conference* (*JIEEEC*), Amman, 16-17 May 2017, 1-6. https://doi.org/10.1109/jieeec.2017.8051400

[29] Peretti, L., Sandulescu, P. and Zanuso, G. (2015) Self-Commissioning of Flux Linkage Curves of Synchronous Reluctance Machines in Quasi-Standstill Condition. *IET Electric Power Applications*, **9**, 642-651. https://doi.org/10.1049/iet-epa.2015.0070

[30] Dhatt, G. and Touzot, G. (1981) Une présentation de la méthode des éléments finis. Presses Université Laval.

[31] Durufle, M. (2006) Intégration numérique et éléments finis d'ordre élevé appliqués aux équations de Maxwell en régime harmonique. PhD Thesis, ENSTA ParisTech.

[32] Bocker, J. (2020) Analysis of the Magnetic Skin Effekt in Motors and Inductors. 2020 *International Symposium on Power Electronics*, *Electrical Drives*, *Automation and Motion* (*SPEEDAM*), Sorrento, 24-26 June 2020, 103-107.
https://doi.org/10.1109/speedam48782.2020.9161895

[33] Ding, Z., Bu, W., Cai, X., Wu, X. and Liu, S. (2019) Finite Element Analysis and Modeling of Three-Phase Induction Motor. *IOP Conference Series*: *Materials Science and Engineering*, **677**, Article 052055. https://doi.org/10.1088/1757-899x/677/5/052055

[34] López-Fernandez, X.M. and Piper, M. (n.d.) Magnetodynamic Performance in Cage Induction Motors with a Broken Bar. In: Wiak, S., Krawczyk, A. and Trlep, M., Eds., *Computer Engineering in Applied Electromagnetism*, Springer-Verlag, 317-322. https://doi.org/10.1007/1-4020-3169-6_55

[35] Papazacharopoulos, Z., Tatis, K., Kladas, A. and Manias, S. (2004) Dynamic Model for Harmonic Induction Motor Analysis Determined by Finite Elements. *IEEE Transactions on Energy Conversion*, **19**, 102-108. https://doi.org/10.1109/tec.2003.821825

[36] Stephen Ejiofor, O., Candidus, E., Stephen, A., Ogbuefi, U. and Peter, U. (2020) Dynamic Modeling and Simulation of 10hp Induction Motor Driving a Variable Load. *International Journal of Engineering & Technology*, **9**, 17-25. https://doi.org/10.14419/ijet.v9i1.30176

[37] Menghal, P.M. and Laxmi, A.J. (2014) Dynamic Modeling, Simulation & Analysis of Induction Motor Drives. 2014 *International Conference on Science Engineering and Management Research* (*ICSEMR*), Chennai, 27-29 November 2014, 1-7. https://doi.org/10.1109/icsemr.2014.7043553

[38] Tahi, S. and Ibtiouen, R. (2014) Finite Element Calculation of the Dq-Axes Inductances and Torque of Synchronous Reluctance Motor. 2014 *International Conference on Electrical Sciences and Technologies in Maghreb* (*CISTEM*), Tunis, 3-6 November 2014, 1-5. https://doi.org/10.1109/cistem.2014.7076979

[39] Luo, W., Wang, B., Zhao, H. and Luo, Y. (2014) Modeling and Simulation of Non-Linear Dynamic Process of the Induction Motor System with Fluctuating Potential Loads. *Science China Technological Sciences*, **57**, 1729-1737. https://doi.org/10.1007/s11431-014-5611-4

[40] Hiswe, F., Effa, J. and Kenmoe, F. (2020) Optimization of Sensorless Field-Oriented Control of an Induction Motor Taking into Account of Magnetic Saturation. *International Journal of Dynamics and Control*, **8**, 229-242.

[41] Avdeev, B.A. and Vyngra, A.V. (2020) Simulation of Variable Frequency Controlled AC Induction Motor Operating on Non-Linear Load. 2020 *IEEE Conference of Russian Young Researchers in Electrical and Electronic Engineering* (*EIConRus*), St. Petersburg and Moscow, 27-30 January 2020, 2346-2349. https://doi.org/10.1109/eiconrus49466.2020.9038963

[42] Alberti, L., Bianchi, N. and Bolognani, S. (2011) Variable-Speed Induction Machine Performance Computed Using Finite-Element. *IEEE Transactions on Industry Applications*, **47**, 789-797. https://doi.org/10.1109/tia.2010.2103914

[43] Melcescu, L.M., Cistelecan, M.V., CRaiu, O. and Cosan, H.B. (2010) A New 4/6 Pole-Changing Double Layer Winding for Three Phase Electrical Machines. *The XIX International Conference on Electrical Machines-ICEM* 2010, Rome, 6-8 September 2010, 1-6. https://doi.org/10.1109/icelmach.2010.5608041

[44] Rezazadeh, G., Tahami, F., Capolino, G., Vaschetto, S., Nasiri-Gheidari, Z. and Henao, H. (2020) Improvement of Concentrated Winding Layouts for Six-Phase Squirrel Cage Induction Motors. *IEEE Transactions on Energy Conversion*, **35**, 1727-1735. https://doi.org/10.1109/tec.2020.2995433

[45] Cistelecan, M.V., Ferreira, F.J.T.E. and Popescu, M. (2010) Three Phase Tooth-Concentrated Interspersed Windings with Low Space Harmonic Content. *The XIX International Conference on Electrical Machines-ICEM* 2010, Rome, 6-8 September 2010, 1-6. https://doi.org/10.1109/icelmach.2010.5608144

[46] Conradi, A., Schmülling, C. and Schmülling, S. (2013) Investigation on the Effects of Magnetic Saturation in Induction Machines during Transients. *GSTF Journal of Engineering Technology*, **2**, 20-29. https://doi.org/10.5176/2251-3701_2.3.87

[47] Troncon, D., Carbonieri, M., Alberti, L. and Bianchi, N. (2021) Measures and Simulations of Induction Machines Flux Linkage Characteristics Based on Rotor Field Orientation. *IEEE Transactions on Industry Applications*, **57**, 4686-4693. https://doi.org/10.1109/tia.2021.3089662

[48] Tuovinen, T., Hinkkanen, M. and Luomi, J. (2008) Modeling of Mutual Saturation in Induction Machines. 2008 *IEEE Industry Applications Society Annual Meeting*, Edmonton, 5-9 October 2008, 1-8. https://doi.org/10.1109/08ias.2008.32

[49] Shi, Y., Sarlioglu, B. and Lorenz, R.D. (2019) Parametric Analysis of Tradeoffs between Transient and Steady-State Loss Reduction for Induction Machines of Different Sizes. 2019 *IEEE Transportation Electrification Conference and Expo* (*ITEC*), Detroit, 19-21 June 2019, 1-6. https://doi.org/10.1109/itec.2019.8790565

[50] Kidd, B. (2022) Vector-Based Magnetic Circuit Modelling of Induction Motors. *Magnetism*, **2**, 130-151. https://doi.org/10.3390/magnetism2020010